



Capturing the continuous complexity of behaviour in *Caenorhabditis elegans*

Tosif Ahamed¹, Antonio C. Costa¹ and Greg J. Stephens^{1,2}✉

Animal behaviour is often quantified through subjective, incomplete variables that mask essential dynamics. Here, we develop a maximally predictive behavioural-state space from multivariate measurements, in which the full instantaneous state is smoothly unfolded as a combination of short-time posture sequences. In the off-food behaviour of the roundworm *Caenorhabditis elegans*, we discover a low-dimensional state space dominated by three sets of cyclic trajectories corresponding to the worm's basic stereotyped motifs: forward, backward and turning locomotion. We find similar results in the on-food behaviour of foraging worms and *npr-1* mutants. In contrast to this broad stereotypy, we find variability in the presence of locally unstable dynamics with signatures of deterministic chaos: a collection of unstable periodic orbits together with a positive maximal Lyapunov exponent. The full Lyapunov spectrum is symmetric with positive, chaotic exponents driving variability balanced by negative, dissipative exponents driving stereotypy. The symmetry is indicative of damped-driven Hamiltonian dynamics underlying the worm's movement control.

Animals move in a wide variety of ways; the complex posture dynamics generating these behaviours span multiple spatio-temporal scales, and exhibit both regularity and variability¹. At large scales, behaviour is structured, organized into stereotyped motifs such as walking or running, but the dynamics within each motif can be highly irregular². This complexity is apparent in spontaneous behaviours³, but also in highly stereotyped sequences such as an ‘escape response’, which must also be unpredictable for successful avoidance of predators⁴. Despite the importance of behaviour in fields ranging from neuroscience⁵, ethology¹, control theory⁶, robotics and artificial intelligence⁷ to the physics of living systems⁸, the complexity of movement presents unique challenges in quantification, analysis and understanding.

Technological advances, including recent progress in machine vision^{9–11}, now make it possible to gather high-resolution movement data, even in complex, naturalistic settings and for animals with intricate body plans^{12,13}. But how do we map high-resolution recordings of animal behaviour into a compressed set of interpretable numbers while retaining maximal information about the dynamics? Indeed, among biological signals, behaviour exhibits a remarkable divergence of descriptions, from representations based on pixels and wavelets¹⁴ to postures^{15,16} to more abstract states¹⁷. Certainly, a good representation should capture the difference between distinct movement patterns. An ideal representation will also allow near-future predictions and be interpretable to provide insight into movement control principles. Finally, we seek to reveal rather than impose the structure of the behavioural signal, letting the representation and analysis guide important characteristics such as continuous versus discrete, variable versus stereotyped and spontaneous versus controlled.

We detail the construction and application of a behavioural-state space inspired by the similar approach of dynamical systems (also known as a phase space^{18,19}, not to be confused with ‘state-space models’ in statistics²⁰). A point in our generally multidimensional behavioural-state space represents the complete, near-instantaneous movements of an animal: posture and short-time posture changes. As time evolves, the state-space point follows a smooth trajectory,

thus providing a geometrical encoding of behaviour. Combining dynamical systems theory with high-resolution posture time series of the nematode *Caenorhabditis elegans*, we exploit the detailed structure of these trajectory encodings to seek a new quantitative perspective of ethological analysis.

State-space reconstruction by maximizing predictability

We consider a d -dimensional time series $y(t)$ of duration T collected in a $T \times d$ matrix Y , which represents noisy, incomplete measurements of an underlying dynamical system (Fig. 1). With a state-space reconstruction, we seek a coordinate transformation Ψ that maps Y into a space X that is topologically equivalent²¹ to the state space of the underlying dynamical system, a process known as time-series embedding^{22,23}. Dynamical embeddings have been used to model complex phenomena such as ecological and neural dynamics^{24,25}, and to characterize the stability and symmetry of their reconstructed attractors²⁶. Although early approaches primarily used single-variable measurements, multivariate embeddings provide better reconstructions²⁷ and can improve prediction²⁸. Our principal example is where Y consists of eigenworm posture measurements ($d=5$) of freely moving worms. The embedding then defines a coordinate system that captures essential information about the underlying neuromuscular dynamics.

In our approach, we first lift the d -dimensional measurements into a Kd -dimensional space of K contiguous delays and then project to a smaller m -dimensional subspace. Formally we decompose the embedding $\Psi = P_m \circ \Phi_K$ into a delay map Φ_K , in which we iteratively stack ($K-1$) delayed copies of Y into a $(T-K+1) \times Kd$ matrix \bar{Y}_K , followed by a dimensionality reduction transformation P_m , which projects \bar{Y}_K onto an $m < Kd$ -dimensional space. P_m can in principle be any transformation and examples include numerical derivatives²⁹, delay coordinates³⁰ and random projections²⁵. Here, we use singular value decomposition (SVD)^{23,27} followed by independent component analysis (ICA)³¹, which results in a state space with independent components spanning the dimensions of the first m singular vectors. In matrix notation $X_m = \bar{Y}_K \Gamma_m$, where Γ_m is the

¹Biological Physics Theory Unit, OIST Graduate University, Okinawa, Japan. ²Department of Physics and Astronomy, Vrije Universiteit Amsterdam, Amsterdam, The Netherlands. ✉e-mail: g.j.stephens@vu.nl

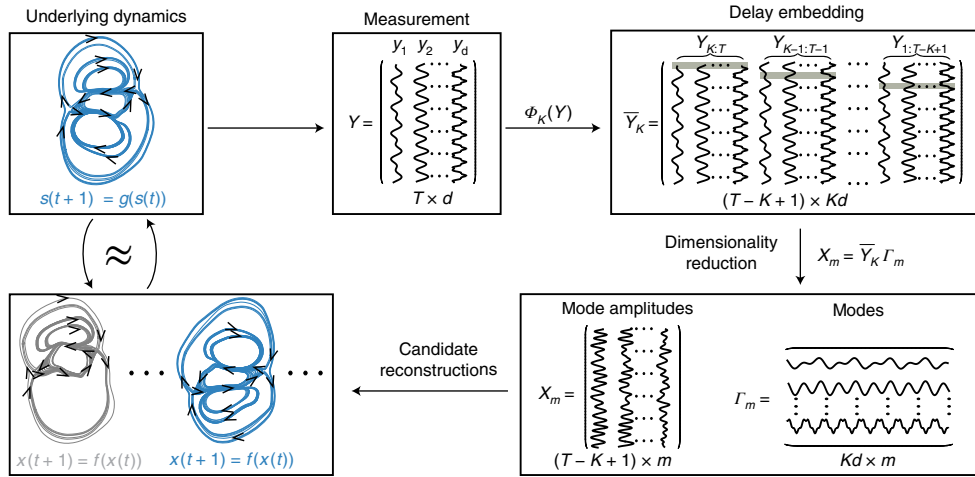


Fig. 1 | State-space reconstruction. From upper left: a d -dimensional time series of an underlying dynamical system is collected in the measurement matrix Y . Φ_K stacks delayed copies of the measurements within a short time window into a matrix \bar{Y} . Dimensionality reduction of \bar{Y} results in an m -dimensional state space spanned by the basis vectors called the modes. The mode coefficients form an approximation of the state space of the underlying dynamics. Each value of K and m results in a different state-space reconstruction of the underlying dynamics and we seek embedding parameters that maximize predictability.

$Kd \times m$ matrix of basis vectors spanning the m -dimensional state space, while X_m contains the state-space trajectories. This space of transformations allows for both derivative and more general linear filters³² and the resulting coordinates reflect the most dominant linear modes of the dynamics^{23,32}.

The reconstruction is parameterized by the window length K and the state-space dimension m , and we describe a new, principled procedure for determining (K, m) on the basis of optimal prediction. Notably, embedding parameters have often been chosen heuristically^{23,32}. To predict future observations we use N_b nearest neighbours in the reconstructed state space (Fig. 2a left). To compute $y_{\text{est}}(t+\tau)$, the τ -step prediction of $y(t)$, we average the future of the nearest neighbours of the corresponding state-space point so that $x_{\text{est}}(t+\tau) = \langle x(t+\tau) \rangle_{N_b}$ and then apply Φ_K^{-1} to pull x_{est} back to observation space. This is known as the nearest-neighbour predictor and also as Lorenz's 'method of analogues'³³. The nearest-neighbour predictor provides a lower bound to the predictability of a state-space reconstruction, as it is equivalent to a zeroth-order Taylor approximation of the dynamics in a local neighbourhood.

We quantify the prediction quality after τ steps using the error

$$E(\tau) = \sum_{j=1}^d \langle (y_j(t'+\tau) - (y_{\text{est}})_j(t'+\tau))^2 \rangle_{t'}^{1/2} \quad (1)$$

as shown in Fig. 2a(middle). Although $E(\tau)$ is a function, we seek a single scalar that captures overall predictability. For a completely predictable system $E(\tau)$ is constant with a value corresponding to the noise level in the observations. On the other hand, for systems where predictions worsen over time, $E(\tau)$ grows according to a non-trivial process, possibly involving multiple timescales^{33,34}, shown schematically in Fig. 2a(right).

As long as the system is stationary, the error is bounded and $E(\tau)$ does not grow indefinitely, but saturates to a value e_s as $\tau \rightarrow \infty$, at which time the predictions are as good as choosing randomly from the sampled state space. We use the cumulative difference between the early-time and asymptotic errors to define T_{pred} as a new measure of predictability,

$$T_{\text{pred}} = \frac{1}{e_s} \int_0^\infty (e_s - E(\tau)) d\tau = \frac{\Delta}{e_s} \quad (2)$$

where Δ is the area between the curve $E(\tau)$ and the asymptote e_s . A state-space reconstruction with a large T_{pred} is good in the sense that it allows us to predict future observations for as long as possible. Although several previous reconstruction studies are based on prediction as a guiding principle, they have used the predictive error in a more ad hoc manner, either by setting τ to a specific value^{22,24}, or by integrating $E(\tau)$ to a chosen time τ_0 (ref. 35).

The average prediction error for an arbitrary time τ' is $\langle E(\tau') \rangle = \frac{1}{\tau} \int_0^{\tau'} E(\tau) d\tau$. At large enough τ' , $E(\tau)$ approaches e_s and we can write $\langle E(\tau') \rangle = e_s - \Delta/\tau'$. Thus, the average prediction error is reduced from its asymptotic limit by an amount given by Δ/τ' . In a densely sampled state space T_{pred} is also the characteristic timescale for the total s.d. of a ball of points to relax to the total s.d. of the state-space distribution.

We demonstrate our embedding approach on a noisy measurement of a single coordinate of the Lorenz system (State-space reconstruction for the Lorenz system simulation) and display the results in Fig. 2b–e. We find that T_{pred} increases with K for $K < 25$ frames, after which it decreases gradually, and we choose $K^* = 25$. We project \bar{Y}_{K^*} on the first m singular vectors and find that T_{pred} decreases after $m^* = 3$.

The low-dimensional state space of *C. elegans* locomotion

We leverage our state-space reconstruction to elucidate the behaviour of the nematode *C. elegans* freely foraging on a flat agar plate^{36,37}. In two dimensions, worms move by making dorsoventral sinusoidal bends along their bodies³⁸, which can be captured through high-resolution tracking microscopy to give a multidimensional time series of posture changes. Despite the variety of visible postures, most of the shape variation is captured by a linear combination of a small number of primitive shape dimensions (eigenworms)^{15,37} (Fig. 3a).

Projections along the eigenworm dimensions describe the worm's instantaneous shape and are not a direct indication of behaviour, which arises from posture changes. Dynamical representations based on derivatives^{15,36,39}, and on sequences of postures^{40,41}, have been used to quantitatively explore the worm's behaviour. Importantly, the low dimensionality of the worm's shape space does not imply simplicity and low dimensionality of the behavioural

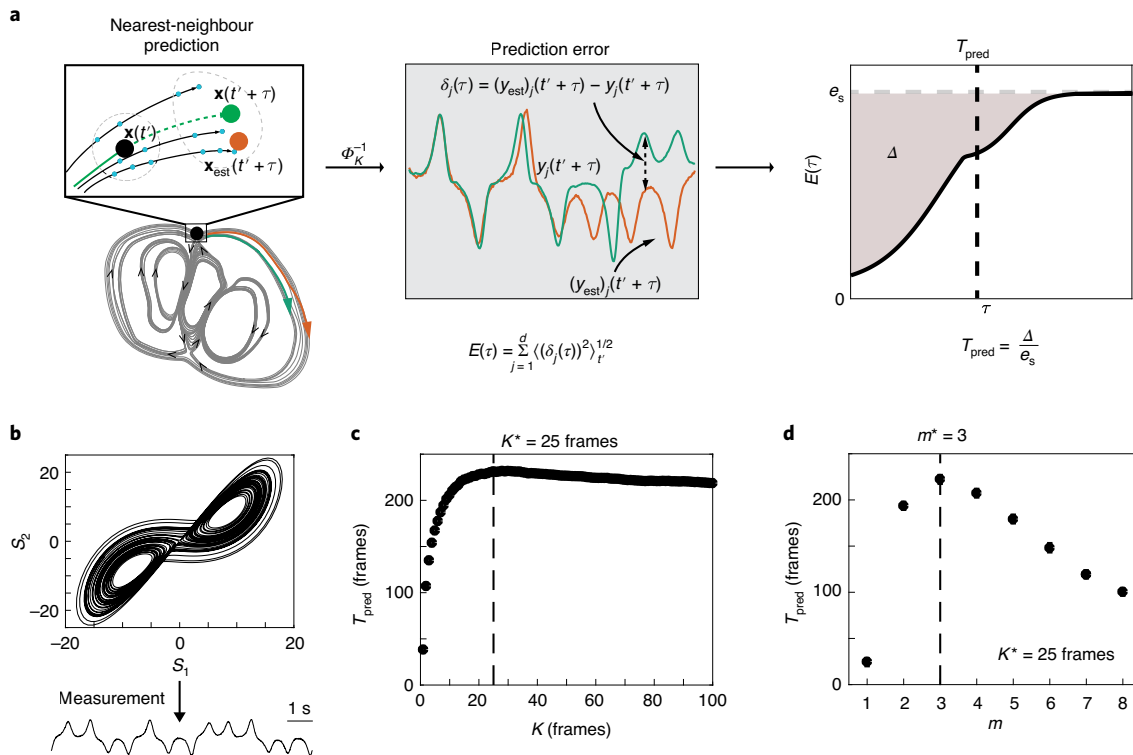


Fig. 2 | Reconstruction parameters for maximum predictability. **a**, We use a nearest-neighbour predictor, which averages the τ -step future of nearest neighbours of a point $\mathbf{x}(t)$ in the candidate reconstruction to estimate future measurements. In general, for stationary complex systems, prediction worsens with time and $E(\tau)$ grows before saturating to e_s , corresponding to the size of the system in state space. **b–d**, We apply our reconstruction to the time series corresponding to a noisy measurement of the first coordinate of the Lorenz system with standard chaotic dynamics. **c**, T_{pred} varies for different K , with a maximum $K^* \approx 0.25 \text{ s}$. **d**, T_{pred} is maximal for the reconstruction defined by K^* and the first three singular vectors, resulting in a three-dimensional embedding of the chaotic attractor, which has fractal dimension $D \approx 2.05$. Error bars in **c** and **d** are comparable to the symbol size.

dynamics, and there are several signs of complexity in *C. elegans* behaviour, such as heavy-tailed distributions⁴⁰, hierarchical structure in posture sequences⁴¹ and indications of dynamical criticality in local linear approximation of the dynamics³⁹, as well as simultaneous presence of stereotypy and variability in posture sequences^{15,36,40}.

To reconstruct the state space of the worm's posture dynamics, we start with a $T \times 5$ measurement matrix Y consisting of five eigenworm coefficients for a recording with $T = 33,600$ frames (sampled at 16 Hz) (Fig. 3a). We stack $K - 1$ time-shifted copies of Y to give the $(T - K + 1) \times 5K$ state matrix \bar{Y}_K . To estimate the optimal window size, we compute T_{pred} for each choice of K , as shown in Fig. 3b for a single representative worm, and choose $K^* = 12$. Within this window, we find that predictability saturates with $m = 7$ singular vectors (Fig. 3c). Analysis of each worm in the foraging dataset reveals a similar simplicity (Extended Data Fig. 1a,b). Despite its observed complexity, worm behaviour is characterized by a low-dimensional state space.

We increase the interpretability of the worm's state-space reconstruction through a final transformation to independent components. We use FastICA³¹ on the $m = 7$ projections of the delay matrix \bar{Y}_{K^*} to obtain independent coordinate directions and we denote these coordinates 'behavioural modes', Γ . We show the seven behavioural modes in Fig. 3d as curvature kymographs and note that they fall into three groups, broadly corresponding to the three coarse categories of worm movement: forward, backward and turning locomotion. Specifically, Γ_{11} and Γ_{12} modes correspond to the ventrally and dorsally initiated anterior-posterior body waves that worms make during forward locomotion. The reversal modes Γ_{r1} and Γ_{r2} capture the posterior-anterior body waves worms make during backward locomotion. Analogous to sine and cosine pairs

of a pure harmonic oscillator, these modes form near-quadrature pairs of oscillations during forward and backward locomotion. Finally, $\{\Gamma_{11}, \Gamma_{12}, \Gamma_{13}\}$ correspond to longer-ranged body bends. Large projections along Γ_{11} and Γ_{12} correspond to bends directed towards the ventral or dorsal direction respectively during a delta-turn-like bend³⁷, while Γ_{13} corresponds to an omega-turn-like bend. In this representation, worm locomotion is approximated by linearly combining these modes with time-varying amplitudes. We find similar modes for different choices of m^* (Extended Data Fig. 2) and also for an ensemble embedding constructed by concatenating all $N = 12$ foraging organisms (Extended Data Figs. 3 and 4). The behavioural modes emerge in an unsupervised manner, with no previous information on the worm's movement.

The topology and geometry of trajectories in the behavioural-state space contain important qualitative and quantitative information about worm behaviour. A 10-min trajectory is visualized in Fig. 3e as projections onto the three mode combinations described above. In the (X_{11}, X_{12}) and (X_{r1}, X_{r2}) planes, trajectories are coloured by the centroid velocity of the worm, negative for backward locomotion and positive for forward locomotion. Trajectories in the (X_{11}, X_{12}, X_{13}) space are coloured by the mean body curvature. Large excitations in each of the three projections correspond to forward, backward and turning locomotion respectively. Specifically, trajectories in the (X_{11}, X_{12}) plane form a prominent circular band indicating nearly constant-amplitude body waves during forward locomotion. Reversals emerge as trajectories spiralling from the centre to a maximum radius in the (X_{r1}, X_{r2}) plane, and then spiralling in as a reversal ends. Finally, deep body bends are represented as large transient orbits, with ventral turns and dorsal turns on opposite sides. Wild-type worms have a ventral bias in their deep body

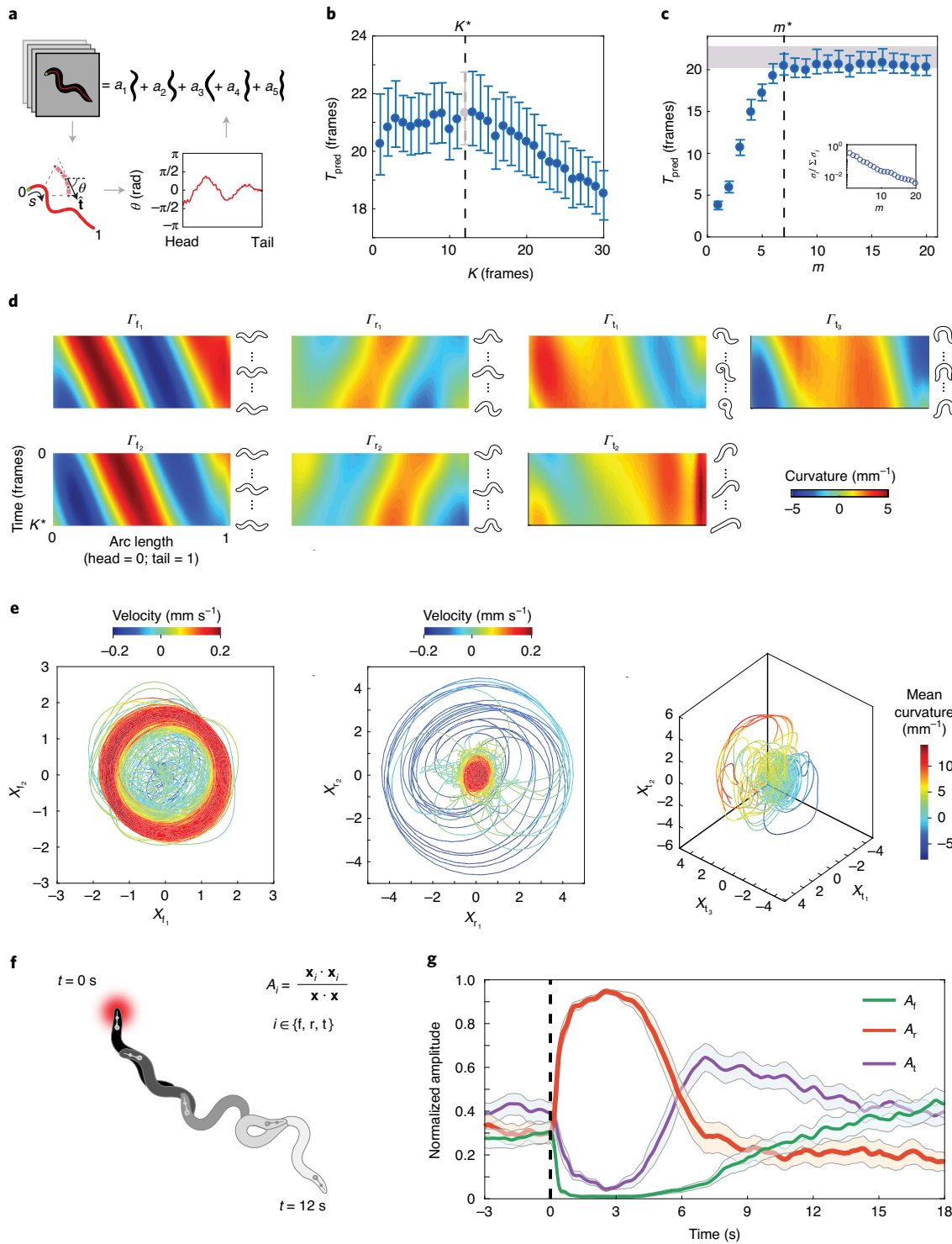


Fig. 3 | The low-dimensional state space of *C. elegans* locomotion. **a**, We parameterize worm posture by eigenworm projections. **b–e**, The embedding process for the foraging behaviour of an example worm. **b**, T_{pred} as a function of K . We set $K^* = 12$, -1/2 cycle of the worm's body wave. **c**, T_{pred} as a function of m . Embeddings with dimensions beyond $m^* = 7$ carry little predictive structure. The grey bar denotes $T_{\text{pred}}(K = K^*)$. Inset: the normalized singular-value spectrum does not show an obvious cutoff. **d**, We decompose the seven-dimensional embedding into linear combinations of independent posture sequences of length K^* , which we denote behavioural modes. We show the modes as curvature kymographs and note that there are two approximately quadrature pairs and a third group with three modes. **e**, Trajectories visualized as projections onto the mode combinations (10 min in duration). In the (X_{t_1}, X_{t_2}) and (X_{r_1}, X_{r_2}) planes, the trajectories are coloured by centroid velocity, negative (blue) for backward locomotion, and positive (red) for forward. Trajectories in the $(X_{t_1}, X_{t_2}, X_{t_3})$ space are coloured by the mean body curvature (blue for dorsal, red for ventral). **f,g**, We apply our embedding to the behaviour of worms escaping from a heat impulse to the head. **f**, Schematic of the response. **g**, We project the escape dynamics using the ensemble foraging modes (Extended Data Fig. 3) and visualize the dynamics through normalized amplitudes of the forward, reverse and turning projections. Reversal dynamics (red) initiate just after the impulse (dotted line), while turning dynamics (purple) are suppressed. The reversal ends with the initiation of an omega-turn. Shaded regions indicate 95% confidence intervals computed by bootstrapping over all recordings in the dataset.

bends, which is visible in the state space as a greater density of orbits on one side of the three-dimensional projection.

The state space also captures relationships between different body wave patterns. For example, we find that most reversals transition to forward by way of a deep ventral bend (Extended Data Fig. 1d), an observation that was previously reported in the context of the escape response and pirouette reorientation sequence^{42,43}. To quantify the relative activity of each set of body waves and the phase relationships between them, we define normalized mode amplitudes, $A_i = \frac{\mathbf{x}_i \cdot \mathbf{x}}{\|\mathbf{x}\|}$, where $i \in \{f, r, t\}$. The A_i range from 0 to 1 and measure the relative activity of different body wave patterns. We use these amplitudes to examine the behaviour of $N=92$ on-food worms where a brief laser impulse is applied to the head, resulting in a localized thermal stimulus provoking an escape response³⁷, shown schematically in Fig. 3f. We project the posture dynamics of each stimulated worm onto the ensemble modes (Extended Data Fig. 3) and show the normalized mode amplitudes averaged across all worms (Fig. 3g). The amplitudes capture the timescales and phase relationships between different body wave patterns during an escape sequence. In particular, the turning modes are strongly suppressed after the initiation of the reversal, increasing gradually as the reversal ends and worms transition into a turn. The turning amplitude then decreases, while forward amplitude increases as worms resume forward movement in the approximately opposite direction.

We extend our analysis to include on-food behaviour of wild-type worms as well as the mutant strain *npr-1* (Extended Data Fig. 5). The movement of wild-type worms on a bacterial lawn is more complex than that seen off food, exhibiting more irregular body motions and including switches between a ‘roaming’ state, where worms explore the food patch by making long forward runs, and a ‘dwelling’ state, where worms exploit a local food patch by limiting their centroid displacement through increased reversals and turning^{17,44} (see also Extended Data Fig. 10a). The neuropeptide receptor NPR-1 is known to affect these foraging behaviours, with *npr-1* mutant worms exhibiting an increased frequency of roaming¹⁵. We find that the dominant on-food modes of roaming wild-type and mutant *npr-1* worms are remarkably similar, both to each other and to the primary off-food modes. The similarity of these embeddings in distinct contexts and imaging environments illustrates the robustness of our technique and also offers new, posture-scale evidence that the NPR-1 mutation overrides the switch to dwelling.

Unstable periodic orbits and deterministic behavioural variability

The state space of worm locomotion is organized such that neighbouring points correspond to similar behavioural sequences of length K . However, these neighbouring sequences diverge with time, resulting in unpredictability, as in the example of Fig. 4a. In particular, the average distance between neighbouring trajectories exhibits a regime of exponential growth (Extended Data Fig. 6a), hinting at a connection to deterministic chaotic dynamics. Chaotic dynamics are also fundamentally tied to collections of unstable periodic orbits (UPOs)⁴⁶, and we note the strong cyclic appearance of trajectories within the projections (Fig. 3e). A number of biological systems have been investigated using periodic orbits, including neuronal activities^{47,48}, human electroencephalograms⁴⁷, crayfish photoreceptors⁴⁹ and cardiac arrhythmias⁵⁰.

We search for periodic orbits by identifying the first recurrence times in a neighbourhood⁵¹. Given a point $\mathbf{x}(i)$ in state space, we find the smallest $k > i$ such that $\mathbf{x}(k)$ is a transverse neighbour of $\mathbf{x}(i)$. The sequence $[\mathbf{x}(i), \mathbf{x}(i+1), \dots, \mathbf{x}(k)]$ is then detected as a periodic orbit of period $p = k - i$ (Periodic orbits). The stability of these periodic orbits is given by their maximal Floquet exponents, which we estimate by computing the maximal expansion rate of a ball of points along the orbit (Floquet exponents). For the Lorenz system, we show that the orbits detected as above agree with the true

periodic orbits taken from high-precision numerical calculations⁵² (Extended Data Fig. 7a–e). The maximal Floquet exponents are also recovered correctly (Extended Data Fig. 7f).

When applied to the state space of foraging worms, we find that the distribution of the number of periodic orbits exhibits peaks at approximately integer multiples of a minimum period p_{\min} corresponding to the frequency of each worm’s body wave during forward locomotion (Fig. 4b inset). We quantify the stability of each periodic trajectory by computing its maximal Floquet exponent. The distribution of Floquet exponents is largely positive, indicating that the worm’s periodic orbits are mostly unstable (Fig. 4b). The UPOs of worm behaviour provide a longer-timescale description of the movement and also a quantitative characterization of the trajectory divergence in Fig. 4a. We estimate the maximal Lyapunov exponent λ_{\max} by an average of the Floquet exponents of periodic orbits of increasing length, weighted by $e^{-\mu_1 p}$, where μ_1 is the maximal Floquet exponent of the orbit, and p is its period⁵³. Including orbits of duration up to $p=8$ (Fig. 4c (blue)) provides an approximation of λ_{\max} , which agrees with direct trajectory divergence estimates averaged across all worms (grey bar, see also Extended Data Fig. 6a and λ_{\max}). The average across random segments of the same length converges more slowly (Fig. 4c (red)).

The detected periodic orbits are interpretable in terms of commonly observed *C. elegans* behaviours. Orbits with p_{\min} correspond to forward and backward crawling including orbits with a dorsal or ventral bias (Extended Data Fig. 8b,c). More surprisingly, longer periodic orbits are composites, corresponding to longer-time reorientation behaviours of the worm’s navigation such as pirouettes and escape strategies^{42,43,54}. In Fig. 4d (blue) we show state-space trajectories of one such period-4 orbit. This orbit is composed of a reversal followed by a deep body bend, and subsequent forward movement: a posture sequence previously reported in pirouette reorientation and escape behaviours^{42,43}. Though this periodic orbit is several body waves long, it is repeated almost exactly at different times during the recording. We show one such recurrence Fig. 4d (orange), along with the corresponding posture sequences. As in the Lorenz system, the presence of UPOs suggests an intriguing view of the worm’s foraging dynamics where the state wanders aperiodically in a complex landscape composed of unstable orbits.

Symmetric Lyapunov spectrum and damped-driven Hamiltonian dynamics

While the behaviour of *C. elegans* is simpler than that of most animals, the quantitative dynamics of worm posture defy a straightforward interpretation, or even as yet a model (see for example ref. ⁵⁵ for a review). There is rough stereotypy in the orbits corresponding to each behaviour, but also large cycle-to-cycle variation. Such variability is linked to a positive maximal Lyapunov exponent and UPOs (Fig. 4b,c and Extended Data Fig. 6a), so that even within a ‘single’ behaviour such as forward crawling each cycle is deterministically different. To more fully illuminate this variability, we examine the dynamics along all dimensions within the state space.

In an m -dimensional state space, local neighbourhoods are sheared by the flow and are simultaneously stretched and squeezed along different directions, dynamics that are invariantly characterized by the Lyapunov exponents, $\lambda_{i=1,\dots,m}$. Such stretching and squeezing is described by the Jacobian $J_{\mathbf{x}(t)}$, which maps an m -dimensional spherical neighbourhood to an m -dimensional ellipsoid. The spectrum of Lyapunov exponents is given by the infinite-time average of the logarithms of the principal axes of the ellipsoid (Fig. 5a). Positive Lyapunov exponents reflect directions along which trajectory bundles expand, while negative exponents reflect shrinking directions.

The Lyapunov exponents reveal important information about the dynamics of a system⁵⁶. The sum of the exponents is the average dissipation rate: zero for conservative systems and negative for

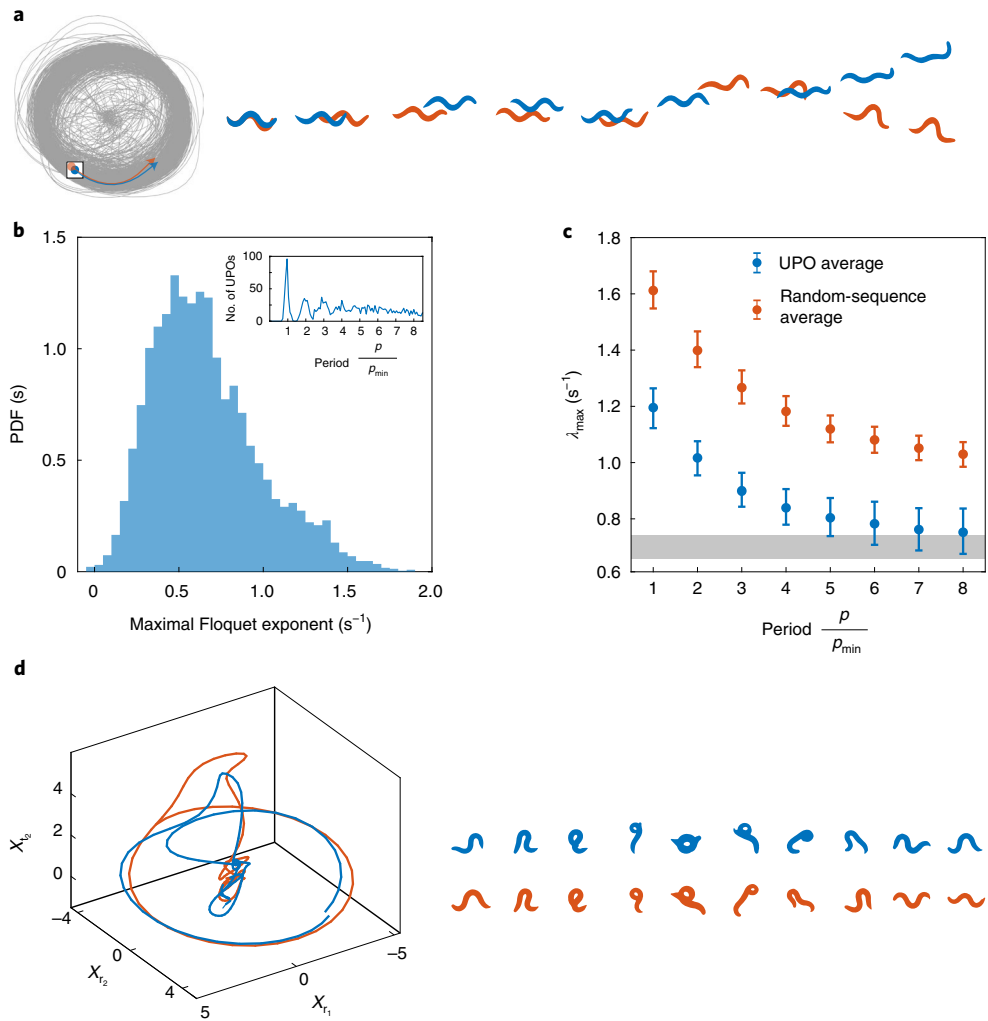


Fig. 4 | Chaotic state-space dynamics reveal a deterministic component of behavioural variability. **a**, Neighbouring state-space points correspond to similar posture sequences, but the futures of these points diverge at longer times. **b**, We identify periodic orbits in the state space using the ensemble embedding and quantify the stability of each periodic orbit through its maximal Floquet exponent. The probability distribution function (PDF) of Floquet exponents shows that the identified periodic orbits are predominantly unstable, as also observed in known chaotic systems. Inset: a histogram of the number of periodic orbits across all worms as a function of their period exhibits peaks at integer multiples of p_{\min} . **c**, We recover the characteristic divergence of the trajectories λ_{\max} (grey bar) by a weighted average of the maximal Floquet exponent across orbits (blue). We quantify the state-space divergence across worms (Extended Data Fig. 6a), and find an exponential regime, yielding an average $\lambda_{\max} = 0.69 (0.65, 0.74) s^{-1}$. In contrast, an average from random sequences of the same length converges more slowly (red). **d**, We show an example period-4 orbit composed of a sequence of reversal, deep body bend and forward movement (blue). This same orbit is revisited at a later time (orange), resulting in a similar sequence of postures for these two long trajectories (right).

those with dissipation. The sum of the positive exponents bounds the metric or Kolmogorov–Sinai entropy rate⁵⁷, providing a principled measure of the unpredictability. In addition, the spectrum of Lyapunov exponents can reveal underlying symmetries and conservation laws. For example, continuous dynamical systems exhibit at least one zero exponent corresponding to time-translation invariance along the direction of the flow.

We compute the Lyapunov spectrum for the state space of *C. elegans* (Lyapunov spectrum and Jacobian estimation), and show bootstrapped density estimates of the $m=7$ exponents across different worms (Fig. 5b). We find two positive exponents, $\lambda_1 = 0.66 (0.62, 0.69) s^{-1}$, $\lambda_2 = 0.29 (0.26, 0.32) s^{-1}$, and a third, near-zero exponent, $\lambda_3 = 0.056 (-0.02, 0.11) s^{-1}$. The Kolmogorov–Sinai entropy rate is thus bounded by the sum of positive exponents as $h_{KS} \leq 1 (0.93, 1.09) \text{ nats s}^{-1}$ (note that we have restored the units of nats for ease of comparison with other entropy

measures). The sum of all of the Lyapunov exponents is negative, indicating that the system is dissipative with a dissipation rate of $\sum \lambda_i = -0.94 (-1.15, -0.78) s^{-1}$. Although trajectory bundles expand locally, dissipation causes them to contract as a whole and relax to an attracting manifold. We estimate the dimension of the attractor as the Kaplan–Yorke dimension $D_{KY} = 5.93 (5.75, 6.08)$ (ref. ⁵⁸). The combination of local expansion generating variability and local contraction generating stereotypy is an essential aspect of the complexity of the worm’s posture dynamics.

The Lyapunov spectrum also exhibits a striking symmetry; exponents come in conjugate pairs that sum to the same number $\alpha = -0.27 (-0.3, -0.24) s^{-1}$ (Fig. 5b inset). The entire spectrum is thus symmetric about α (dotted line). The symmetry is also present in six- and eight-dimensional embeddings (Extended Data Fig. 6b–d). Symmetric Lyapunov spectra have been previously observed in the following damped–driven Hamiltonian systems: a sinusoidally

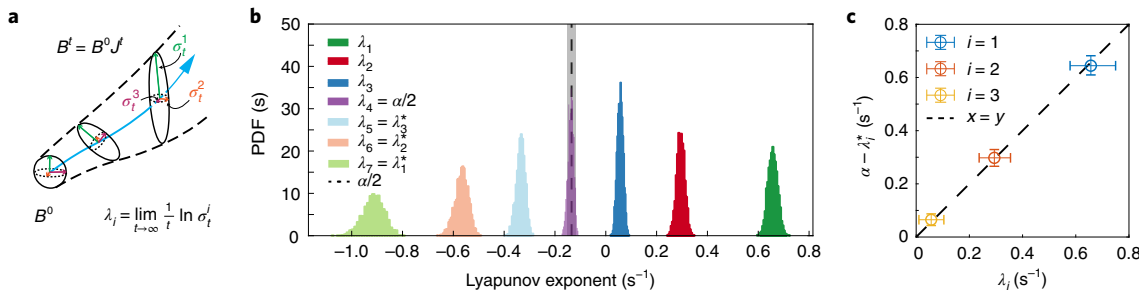


Fig. 5 | A symmetric Lyapunov spectrum indicates damped-driven Hamiltonian dynamics. **a**, The contraction and expansion of local volumes, suitably averaged across the full state space, provides important dynamical invariants and is quantified by a collection of exponents: the Lyapunov spectrum. We sketch the transformation of an initial volume B^0 to a new volume B^t by the flow (blue curve) and the local Jacobian J^t . The spectrum of Lyapunov exponents is given by the size of the principal axes of B^t for $t \rightarrow \infty$. **b**, The Lyapunov spectrum for *C. elegans* foraging dynamics where the distribution for each exponent is constructed from bootstrap samples across different worms. We find two positive (chaotic) exponents driving variability, a near-zero exponent indicative of continuous (non-noisy) dynamics and four negative exponents, which drive stereotypy. The spectrum is symmetric about the point $\alpha/2$, which coincides with λ_4 . **c**, Lyapunov exponents come as conjugate pairs that sum to α , a symmetry suggestive of a damped-driven Hamiltonian system. Error bars show 95% confidence intervals bootstrapped across all worms in the dataset.

driven pendulum with a damping coefficient α (ref. ⁵⁹), coupled Duffing oscillators with viscous damping of α per degree of freedom and a periodic drive⁶⁰ and thermostatted molecular dynamic simulations where α is a feedback friction force per degree of freedom that acts to maintain a dynamic equilibrium by either keeping the kinetic or total energy of the particles constant⁶¹. In contrast, chaotic systems that are not derived from a Hamiltonian, such as the Lorenz and Rössler systems, do not possess a symmetric Lyapunov spectrum. Interestingly, in a biomechanical model of larval *Drosophila* locomotion, damped-driven Hamiltonian chaotic dynamics were sufficient to generate realistic forward and backward crawling, as well as more complex reorientation behaviours⁶².

Discussion

We use sequences of multidimensional data to reconstruct a maximally predictive state space (Figs. 1 and 2). Our reconstruction is made possible by a new measure of predictability, T_{pred} which quantifies the timescale at which predictions of the future randomize according to the state-space density. Conceptually, our approach is a timescale separation; short-time sequences define the reconstructed state variables while longer-time dynamics are encoded as state-space trajectories. Our reconstruction explicitly seeks the full state information available in short-time dynamics, analogous to discovering the additional variable of velocity from the displacement time series of a simple oscillator. Such information is often added implicitly, for example through the choice of derivative filters in neural imaging^{63,64}. Both the resulting state variables and the geometry and topology of their trajectories offer important, coordinate-invariant understanding of the processes generating the dynamics.

In the posture time series of the roundworm *C. elegans* we found that the state space for off-food foraging is dominated by a seven-dimensional basis of interpretable modes Γ (Fig. 3) and their coefficients X , which are qualitatively similar for different worms under the same conditions. These dominant modes also appear in on-food foraging of wild-type and *npr-1* mutant worms. In the ensemble embeddings of off-food worms and the combined embedding of on-food roaming and dwelling worms, we see a similar behaviour in T_{pred} ; most predictive ability is captured within the seven-dimensional space, but there are about six additional modes with small but notable increase in T_{pred} . Both dwelling behaviour (on food) or area-restricted search (off food) offer promising conditions in which to explore the meaning of these additional modes.

Higher-dimensional embeddings or different behavioural modes may also appear in settings we have not analysed.

The behavioural modes could be broadly categorized into groups corresponding to forward, backward and turning locomotion, as well as head dynamics, which was only seen on food. Biologically, these can be linked to known classes of motor neurons: A and B ventral cord motor neurons, which drive backward and forward locomotion respectively, sublateral motor neurons such as SMB and SMD, which control deep body bends, and head motor neurons driving the head muscles⁶⁵. Interestingly, excitatory classes of ventral cord motor neurons were recently reported to be capable of spontaneous rhythm generation and proposed to be central pattern generators for forward and backward locomotion^{66,67}. Although we focused on characterizing the seven-dimensional embedding, similar results are also found in six and eight dimensions (Extended Data Figs. 2–4).

In our embeddings, the state-space trajectories retained large variability, occupying much of the volume in the reconstructed space. A measure of this volume is the Kaplan–Yorke dimension, and we find $D_{\text{KY}} \sim 6$, not substantially smaller than the embedding dimension. One hypothesis for this variability is that worm behaviour is stochastic and results from noise-induced transitions between a finite number of elements such as stable limit cycles representing individual stereotyped motifs^{36,68}. However, the exponential divergence of nearby state-space trajectories (Extended Data Fig. 6a) and the consistency of this divergence with the spectrum of UPOs (Fig. 4), as well as the symmetric Lyapunov spectrum (Fig. 5), provide evidence for important, deterministic variation and cannot be easily explained by a completely stochastic model. From the perspective of deterministic chaos, behavioural dynamics are an aperiodic wandering among an infinite number of UPOs, allowing an animal to generate an infinite number of behavioural sequences. Indeed, this agrees with the finding that the number of novel sequences in *C. elegans* behaviour grows with the observation time⁴⁰. On the other hand, stereotyped trajectories can emerge naturally as orbits with low values of the maximal Floquet exponent. Such trajectories can also be generated by stabilizing periodic orbits with control, for example a simple linear controller of the form $K[g(t) - \mathbf{x}(t)]$, where $g(t)$ are the desired goal dynamics, $\mathbf{x}(t)$ is the current state and K is a control gain matrix⁶⁹. This deterministic picture could lead to important insights into the mechanisms underlying short-time control of behaviour by providing a better interpretation of continuous-time neural recordings or through the

development of precise state-dependent perturbations in the neighbourhood of different unstable periodic orbits.

The symmetric form of the Lyapunov spectrum suggests that the worm's behavioural dynamics can be interpreted as normal modes of a system of coupled, damped and driven, Hamiltonian oscillators,

$$\begin{aligned}\dot{Q}_i &= \frac{\partial H}{\partial P_i} \\ \dot{P}_i &= -\frac{\partial H}{\partial Q_i} + C(Q_i, P_i, \psi(t))\end{aligned}\quad (3)$$

where (Q_i, P_i) are the generalized position and momentum coordinates for the i th normal mode. The Hamiltonian is a scalar function governing the time-independent dynamics resulting from the mechanics of the worm's elastic body; for example, most biomechanical models implement the worm's body mechanics through elastic elements or mechanical linkages, the dynamics of which can be encoded in a Hamiltonian. The term $C(Q_i, P_i, \psi(t))$ encapsulates the time-dependent neuromuscular control forces due to interaction of the worm's body with the environment, proprioceptive feedback and neural processing of various sensory stimuli $\psi(t)$. Interestingly, multiple efforts have reported that various biomechanical measures remain roughly constant across a range of external loads during *C. elegans* locomotion, such as the normalized wavelength of the body wave, angle of attack, bending power, and phase relationship between the muscle activity and body curvature^{70–72}. Following the example of thermostatted dynamics (designed to capture constant-temperature dynamics⁶¹), such emergent constants could be explained through feedback control arising from proprioceptive feedback, which is thought to underlie gait modulation in *C. elegans*^{73,74}. Our work also allows for connections between non-equilibrium thermodynamics and worm behaviour. For example, worm dynamics breaks the Hamiltonian time-reversible symmetry in a continuous fashion via the dissipation rate α , which sets the characteristic timescale at which dynamics can be considered time-reversible symmetric. In addition, the sum of Lyapunov exponents is an estimate of the entropy production rate⁷⁵.

The dynamical invariants such as Lyapunov exponents, dimensions and entropies made accessible by our embedding approach provide important constraints and new understanding for short-time behaviour consisting of neuromuscular control along with the biomechanics of the body and its environmental interaction. However, longer timescales are also present in the short periodic orbits, which are interpretable in terms of behavioural motifs such as forward/backward locomotion, and also longer-time reorientation sequences such as pirouettes. Longer timescales can also be addressed through a systematic coarse-graining of the continuous state-space dynamics, which results in a transfer operator⁷⁶. In this approach the partition itself subsumes much of the nonlinearity so the eigenvalues of the transfer operator can provide a systematic and useful timescale separation. In contrast, linear measures such as the power spectrum are often not informative on the original dynamics of complex systems.

While we expect a dynamical systems perspective to be generally useful in understanding natural behaviour, the analysis here benefits from the relative simplicity of the worm's foraging dynamics and the resulting interpretability of the modes. Though other settings and organisms may generate more complex embeddings, important dynamical information such as trajectory stability and dynamical invariants can still be extracted from the state-space reconstruction. Embedding ideas have also been recently used to understand the global brain dynamics of *C. elegans*⁷⁷ and to identify metastable sets and slow order parameters from molecular dynamics simulations using Markov operators⁷⁸. Our reconstruction framework, including T_{pred} and its estimation, is also applicable to stochastic dynamical systems (work in progress).

Across wide areas of science there has been a remarkable increase in the availability of precise, multidimensional and dynamical data, and new analysis ideas are emerging^{39,79}. Here, we improve on the previous work on state-space reconstruction³⁰ (see also the section 'Worm state-space reconstruction'), where much was in the context of either univariate measurements or known dynamical systems and included a heuristic search of reconstruction parameters. However, challenges associated with high dimensionality, data sampling and non-stationarity remain. For example, the one-step error for N samples from a D -dimensional dynamical system is $E(1)/e_s \approx N^{-1/D}$ (ref. ⁸⁰)—higher-dimensional systems require exponentially more data to keep $E(1)/e_s \ll 1$. A related difficulty is the Euclidean metric used to find nearest-neighbour distances, which is invalid even in lower-dimensional spaces with large curvature fluctuations. In this setting, it might be possible to use metric-learning algorithms⁸¹ to recover a suitable metric from data. Finally, recent progress in leveraging artificial neural networks to recover dynamical invariants⁸² offers promising directions for combining a principled dynamical perspective with high-dimensional, real-world systems.

Online content

Any methods, additional references, Nature Research reporting summaries, source data, extended data, supplementary information, acknowledgements, peer review information; details of author contributions and competing interests; and statements of data and code availability are available at <https://doi.org/10.1038/s41567-020-01036-z>.

Received: 27 November 2019; Accepted: 13 August 2020;

Published online: 05 October 2020

References

- Berman, G. J. Measuring behavior across scales. *BMC Biol.* **16**, 23 (2018).
- Newell, K. & Corcos, D. *Variability and Motor Control* (Human Kinetics, 1993); <https://books.google.co.jp/books?id=gUgQAQAAQAAJ>
- Maye, A., Hsieh, C.-h., Sugihara, G. & Brembs, B. Order in spontaneous behavior. *PLoS ONE* **2**, e443 (2007).
- Moore, T. Y., Cooper, K. L., Biwener, A. A. & Vasudevan, R. Unpredictability of escape trajectory explains predator evasion ability and microhabitat preference of desert rodents. *Nat. Commun.* **8**, 440 (2017).
- Krakauer, J. W., Ghazanfar, A. A., Gomez-Marin, A., MacIver, M. A. & Poeppel, D. Neuroscience needs behavior: correcting a reductionist bias. *Neuron* **93**, 480–490 (2017).
- Cowan, N. J. et al. Feedback control as a framework for understanding tradeoffs in biology. *Am. Zool.* **54**, 223–237 (2014).
- Aguilar, J. et al. A review on locomotion robophysics: the study of movement at the intersection of robotics, soft matter and dynamical systems. *Rep. Prog. Phys.* **79**, 110001 (2016).
- Brown, A. E. X. & de Bivort, B. Ethology as a physical science. *Nat. Phys.* **14**, 653–657 (2018).
- Alexander, M. et al. DeepLabCut: markerless pose estimation of user-defined body parts with deep learning. *Nat. Neurosci.* **21**, 1281–1289 (2018).
- Talmo D, P. et al. Fast animal pose estimation using deep neural networks. *Nat. Methods* **16**, 117–125 (2019).
- Hebert, L., Ahamed, T., Costa, A. C., O'Shaughnessy, L. & Stephens, G. J. WormPose: image synthesis and convolutional networks for pose estimation in *C. elegans*. Preprint at <https://www.biorxiv.org/content/early/2020/07/10/2020.07.09.193755> (2020).
- Graving, J. M. et al. DeepPoseKit: a software toolkit for fast and robust animal pose estimation using deep learning. *eLife* **8**, e47994 (2019).
- Wiltshko, A. B. et al. Mapping sub-second structure in mouse behavior. *Neuron* **88**, 1121–1135 (2015).
- Berman, G. J., Choi, D. M., Bialek, W. & Shaevitz, J. W. Mapping the stereotyped behaviour of freely moving fruit flies. *J. R. Soc. Interface* **11**, 20140672–12 (2014).
- Stephens, G. J., Johnson-Kerner, B., Bialek, W. & Ryu, W. S. Dimensionality and dynamics in the behavior of *C. elegans*. *PLoS Comput. Biol.* **4**, e1000028 (2008).
- Szigeti, B., Deogade, A. & Webb, B. Searching for motifs in the behaviour of larval *Drosophila melanogaster* and *Caenorhabditis elegans* reveals continuity between behavioural states. *J. R. Soc. Interface* **12**, 20150899 (2015).

17. Steven W. F. et al. Serotonin and the neuropeptide PDF initiate and extend opposing behavioral states in *C. elegans*. *Cell* **154**, 1023–1035 (2013).
18. Strogatz, S. H. *Nonlinear Dynamics and Chaos with Student Solutions Manual: with Applications to Physics, Biology, Chemistry, and Engineering* (CRC Press, 2018).
19. Nolte, D. D. The tangled tale of phase space. *Phys. Today* **63**, 33–38 (2010).
20. Durbin, J. & Koopman, S. J. *Time Series Analysis by State Space Methods* (Oxford Univ. Press, 2012).
21. Palis, J. & de Melo, W. *Geometric Theory of Dynamical Systems* (Springer, 1982).
22. Casdagli, M., Eubank, S., Farmer, J. D. & Gibson, J. State space reconstruction in the presence of noise. *Physica D* **51**, 52–98 (1991).
23. Broomhead, D. S. & King, G. P. Extracting qualitative dynamics from experimental data. *Physica D* **20**, 217–236 (1986).
24. Sugihara, G. & May, R. M. Nonlinear forecasting as a way of distinguishing chaos from measurement error in time series. *Nature* **344**, 734 (1990).
25. Tajima, S., Yanagawa, T., Fujii, N. & Toyozumi, T. Untangling brain-wide dynamics in consciousness by cross-embedding. *PLoS Comput. Biol.* **11**, e1004537 (2015).
26. Kantz, H. & Schreiber, T. *Nonlinear Time Series Analysis* Vol. 7 (Cambridge Univ. Press, 2004).
27. Read, P. Phase portrait reconstruction using multivariate singular systems analysis. *Physica D* **69**, 353–365 (1993).
28. Ye, H. & Sugihara, G. Information leverage in interconnected ecosystems: overcoming the curse of dimensionality. *Science* **353**, 922–925 (2016).
29. Packard, N. H., Crutchfield, J. P., Farmer, J. D. & Shaw, R. S. Geometry from a time series. *Phys. Rev. Lett.* **45**, 712 (1980).
30. Takens, F. Detecting strange attractors in turbulence. *Dyn. Syst. Turbul.* **898**, 366–381 (1981).
31. Hyvärinen, A. Fast and robust fixed-point algorithms for independent component analysis. *IEEE Trans. Neural Netw.* **10**, 626–634 (1999).
32. Gibson, J. F., Doyne Farmer, J., Casdagli, M. & Eubank, S. An analytic approach to practical state space reconstruction. *Physica D* **57**, 1–30 (1992).
33. Lorenz, E. Predictability: a problem partly solved. In *Seminar on Predictability, 4–8 September 1995* Vol. 1, 1–18 (ECMWF, 1995); <https://www.ecmwf.int/node/10829>
34. Aurell, E., Boffetta, G., Crisanti, A., Paladin, G. & Vulpiani, A. Predictability in the large: an extension of the concept of Lyapunov exponent. *J. Phys. A* **30**, 1–26 (1997).
35. Judd, K. & Mees, A. Embedding as a modeling problem. *Physica D* **120**, 273–286 (1998).
36. Stephens, G. J., Bueno de Mesquita, M., Ryu, W. S. & Bialek, W. Emergence of long timescales and stereotyped behaviors in *Caenorhabditis elegans*. *Proc. Natl Acad. Sci. USA* **108**, 7286–7289 (2011).
37. Broekmans, O. D., Rodgers, J. B., Ryu, W. S. & Stephens, G. J. Resolving coiled shapes reveals new reorientation behaviors in *C. elegans*. *eLife* **5**, e17227 (2016).
38. Croll, N. A. Behavioural analysis of nematode movement. *Adv. Parasitol.* **13**, 71–122 (1975).
39. Costa, A. C., Ahamed, T. & Stephens, G. J. Adaptive, locally linear models of complex dynamics. *Proc. Natl Acad. Sci. USA* **116**, 1501–1510 (2019).
40. Schwarz, R. F., Branicky, R., Grundy, L. J., Schafer, W. R. & Brown, A. E. X. Changes in postural syntax characterize sensory modulation and natural variation of *C. elegans* locomotion. *PLoS Comput. Biol.* **11**, e1004322 (2015).
41. Gomez-Marin, A., Stephens, G. J. & Brown, A. E. X. Hierarchical compression of *Caenorhabditis elegans* locomotion reveals phenotypic differences in the organization of behaviour. *J. R. Soc. Interface* **13**, 20160466 (2016).
42. Donnelly, J. L. et al. Monoaminergic orchestration of motor programs in a complex *C. elegans* behavior. *PLoS Biol.* **11**, e1001529 (2013).
43. Gray, J. M., Hill, J. J. & Bargmann, C. I. A circuit for navigation in *Caenorhabditis elegans*. *Proc. Natl Acad. Sci. USA* **102**, 3184–3191 (2005).
44. Ben Arous, J., Laffont, S. & Chatenay, D. Molecular and sensory basis of a food related two-state behavior in *C. elegans*. *PLoS ONE* **4**, e7584 (2009).
45. Stern, S., Kirst, C. & Bargmann, C. I. Neuromodulatory control of long-term behavioral patterns and individuality across development. *Cell* **171**, 1649–1662 (2017).
46. Banks, J., Brooks, J., Cairns, G., Davis, G. & Stacey, P. On Devaney's definition of chaos. *Am. Math. Mon.* **99**, 332–334 (1992).
47. So, P., Francis, J. T., Netoff, T. I., Gluckman, B. J. & Schiff, S. J. Periodic orbits: a new language for neuronal dynamics. *Biophys. J.* **74**, 2776–2785 (1998).
48. Mishra, N., Hasse, M., Biswal, B. & Singh, H. P. Reliability of unstable periodic orbit based control strategies in biological systems. *Chaos* **25**, 043104 (2015).
49. Pei, X. & Moss, F. Characterization of low-dimensional dynamics in the crayfish caudal photoreceptor. *Nature* **379**, 618 (1996).
50. Schiff, S. J. et al. Controlling chaos in the brain. *Nature* **370**, 615 (1994).
51. Lathrop, D. P. & Kostelich, E. J. Characterization of an experimental strange attractor by periodic orbits. *Phys. Rev. A* **40**, 4028 (1989).
52. Barrio, R., Dena, A. & Tucker, W. A database of rigorous and high-precision periodic orbits of the Lorenz model. *Comput. Phys. Commun.* **194**, 76–83 (2015).
53. Cvitanović, P. Invariant measurement of strange sets in terms of cycles. *Phys. Rev. Lett.* **61**, 2729 (1988).
54. Pierce-Shimomura, J. T., Morse, T. M. & Lockery, S. R. The fundamental role of pirouettes in *Caenorhabditis elegans* chemotaxis. *J. Neurosci.* **19**, 9557–9569 (1999).
55. Gjorgieva, J., Biron, D. & Haspel, G. Neurobiology of *Caenorhabditis elegans* locomotion: where do we stand? *Bioscience* **64**, 476–486 (2014).
56. Pikovsky, A. & Politi, A. *Lyapunov Exponents: a Tool to Explore Complex Dynamics* (Cambridge Univ. Press, 2016).
57. Young, L.-S. Dimension, entropy and Lyapunov exponents. *Ergod. Theory Dyn. Syst.* **2**, 109–124 (1982).
58. Fredericksen, P., Kaplan, J. L., Yorke, E. D. & Yorke, J. A. The Liapunov dimension of strange attractors. *J. Differ. Equ.* **49**, 185–207 (1983).
59. Sprott, J. C. *Elegant Chaos* (World Scientific, 2010).
60. Dressler, U. Symmetry property of the Lyapunov spectra of a class of dissipative dynamical systems with viscous damping. *Phys. Rev. A* **38**, 2103 (1988).
61. Dettmann, C. P. & Morriss, G. Proof of Lyapunov exponent pairing for systems at constant kinetic energy. *Phys. Rev. E* **53**, R5545 (1996).
62. Loveless, J., Lagogiannis, K. & Webb, B. Modelling the mechanics of exploration in larval *Drosophila*. *PLoS Comput. Biol.* **15**, e1006635 (2019).
63. Kato, S. et al. Global brain dynamics embed the motor command sequence of *Caenorhabditis elegans*. *Cell* **163**, 656–669 (2015).
64. Chen, X., Randi, F., Leifer, A. M. & Bialek, W. Searching for collective behavior in a small brain. *Phys. Rev. E* **99**, 052418 (2019).
65. Cook, S. J. et al. Whole-animal connectomes of both *Caenorhabditis elegans* sexes. *Nature* **571**, 63–71 (2019).
66. Gao, S. et al. Excitatory motor neurons are local oscillators for backward locomotion. *eLife* **7**, e29915 (2018).
67. Xu, T. et al. Descending pathway facilitates undulatory wave propagation in *Caenorhabditis elegans* through gap junctions. *Proc. Natl Acad. Sci. USA* **115**, E4493–E4502 (2018).
68. Revzen, S. & Guckenheimer, J. M. Finding the dimension of slow dynamics in a rhythmic system. *J. R. Soc. Interface* **9**, 957–971 (2011).
69. Jackson, E. A. The OPCL control method for entrainment, model-resonance, and migration actions on multiple-attractor systems. *Chaos* **7**, 550–559 (1997).
70. Fang-Yen, C. et al. Biomechanical analysis of gait adaptation in the nematode *Caenorhabditis elegans*. *Proc. Natl Acad. Sci. USA* **107**, 20323–20328 (2010).
71. Backholm, M., Kasper, A., Schulman, R., Ryu, W. & Dalnoki-Veress, K. The effects of viscosity on the undulatory swimming dynamics of *C. elegans*. *Phys. Fluids* **27**, 091901 (2015).
72. Butler, V. J. et al. A consistent muscle activation strategy underlies crawling and swimming in *Caenorhabditis elegans*. *J. R. Soc. Interface* **12**, 20140963 (2015).
73. Boyle, J. H., Berri, S. & Cohen, N. Gait modulation in *C. elegans*: an integrated neuromechanical model. *Front. Comput. Neurosci.* **6**, 10 (2012).
74. Wen, Q. et al. Proprioceptive coupling within motor neurons drives *C. elegans* forward locomotion. *Neuron* **76**, 750–761 (2012).
75. Daems, D. & Nicolis, G. Entropy production and phase space volume contraction. *Phys. Rev. E* **59**, 4000 (1999).
76. Bollt, E. M. & Santitissadeekorn, N. *Applied and Computational Measurable Dynamics* Vol. 18 (SIAM, 2013).
77. Brennan, C. & Proekt, A. A quantitative model of conserved macroscopic dynamics predicts future motor commands. *eLife* **8**, e46814 (2019).
78. Pérez-Hernández, G., Paul, F., Giorgino, T., De Fabritiis, G. & Noé, F. Identification of slow molecular order parameters for Markov model construction. *J. Chem. Phys.* **139**, 015102 (2013).
79. Brunton, S. L. & Kutz, J. N. *Data-Driven Science and Engineering: Machine Learning, Dynamical Systems, and Control* (Cambridge Univ. Press, 2019).
80. Farmer, J. D. & Sidorowich, J. J. Predicting chaotic time series. *Phys. Rev. Lett.* **59**, 845 (1987).
81. Xing, E. P., Jordan, M. I., Russell, S. J. & Ng, A. Y. Distance metric learning with application to clustering with side-information. In *Advances in Neural Information Processing Systems 15* 521–528 (MIT Press, 2003).
82. Pathak, J., Lu, Z., Hunt, B. R., Girvan, M. & Ott, E. Using machine learning to replicate chaotic attractors and calculate Lyapunov exponents from data. *Chaos* **27**, 121102 (2017).

Publisher's note Springer Nature remains neutral with regard to jurisdictional claims in published maps and institutional affiliations.

© The Author(s), under exclusive licence to Springer Nature Limited 2020

Methods

Software. Code for all analysis reported here was written in MATLAB⁸³ and is publicly available: <https://bitbucket.org/tosifahamed/behavioral-state-space>.

Experimental details. The foraging and escape-response datasets were previously analysed using classical image analysis techniques^{36,37}. Data for N2 worms on food and *npr-1* mutants were collected from an open-access dataset⁸⁴, and analysed to solve for coiled postures with custom-made machine vision algorithms (manuscript in preparation). Mode time series for on-food data are available in the bitbucket above.

Off-food N2 dataset. $N=12$ L4-stage N2 worms were recorded at 32 Hz with high-resolution tracking microscopy. For the analysis here the data were downsampled to 16 Hz. Worms were cultivated under standard conditions at 20 °C (ref. ⁸⁵). Before the assay, worms were cleaned of *E. coli* bacteria by a 1-min immersion in NGM (nematode growth medium) buffer. Worms were then placed on a 9.1-cm assay plate (Petri dish) with a 5-cm-radius copper ring pressed into the agar surface for confinement. The assay started 5 min after the transfer and lasted 35 min.

Escape-response N2 dataset. $N=92$ mid- to late-L4-stage N2 worms were targeted on the head with a 100-ms, 75-mA infrared laser pulse from a diode laser (wavelength 1,440 nm), resulting in a localized temperature change of approximately 0.5 °C. Images were recorded at 20 Hz for 30 s (10 s before stimulation and 20 s after stimulation). To prevent adaptation each worm was only assayed once. To match the sampling rate of the foraging dataset, the posture time series was interpolated and downsampled to 16 Hz using the MATLAB⁸³ resample command.

On-food N2 dataset. $N=50$ adult N2 recordings were collected from an open-access dataset⁸⁴. Worms were grown at room temperature ~22 °C and maintained on standard NGM plates⁸⁶ with three drops of OP50 bacteria. The 3.5-cm low-peptone NGM imaging plates were seeded with 20 µl of OP50, in the centre of the plate, and allowed to dry: the drop of OP50 is nearly circular and ~8 mm in diameter. Worms were then transferred to the centre of the plate, one worm per plate, and given 30 min of habituation, after which they were tracked for 15 min. Worms were imaged on an immobile platform isolated from tracking motion⁸⁷. The sampling rate varies across the open-access dataset, but was 30 Hz in our 50-worm population. Our selected population consists of 25 worms with a higher fraction of roaming states and 25 worms with a higher fraction of dwelling states, classified according to their centroid speed and angular speed averaged in 10-s windows¹⁷ (Extended Data Fig. 10a).

On-food *npr-1* mutant dataset. $N=7$ adult *npr-1* recordings were collected from an open-access dataset⁸⁴. Experimental details and image processing are the same as for the N2 data on food, except that the sampling rate was 20 Hz.

Image analysis and posture-space estimation. For the foraging and escape-response datasets, the image analysis pipeline follows³⁷. Briefly, we parameterize the shape of a worm by tangent angles calculated at 100 points along the body image skeleton. For a recording session of T frames, this results in a $T \times 100$ matrix Θ , containing the shape information for each uncrossed frame where the worm's body does not intersect itself. Next, a five-dimensional approximation of the 100-dimensional posture space is calculated by projecting the elements of Θ onto the basis given by the first five singular vectors (eigenworms) of Θ . For frames with a body crossing, an inverse tracking algorithm is used to identify the eigenworm projections³⁷. For the data collected from ref. ⁸⁴, we used a custom-made machine-vision algorithm¹¹ to resolve blurry frames and coiled postures.

Worm state-space reconstruction. Our reconstruction method improves upon previous reconstruction-method work^{88–91} by proposing a principled scheme for selecting reconstruction parameters on the basis of maximizing predictability. Given a d -dimensional time series in $Y = [y_1^{1:T}, \dots, y_d^{1:T}]$, along with an estimate of the optimal embedding window K^* , and minimum embedding dimension m^* , the state-space reconstruction proceeds as follows. First, we create the $L \times K^*$ matrix \bar{Y}_{K^*} containing delayed copies of the mean-subtracted measurements, $\bar{Y}_{K^*} = [y_{1:d}^{1:L}, y_{1:d}^{2:(L+1)}, \dots, y_{1:d}^{K^*:T}]$, where $L = (T - K^* + 1)$. For the postures of *C. elegans*, the measurements are composed of $d=5$ eigenworm coefficients. Next, we perform ICA on the space formed by the first m^* singular vectors of \bar{Y}_{K^*} using the FastICA algorithm³¹ to obtain an m^* -dimensional state space spanned by the independent basis vectors Γ . Projections of \bar{Y}_{K^*} on the state space are contained in the $L \times m^*$ state-space matrix X . Each row, $x(t)$, of X is the behavioural state encoding the instantaneous behaviour of the worm at time t , while the temporal sequence, $[x(t), \dots, x(t+\tau)]$, forms a continuous trajectory in state space that encodes the shape change dynamics of a behavioural sequence.

State-space reconstruction for the Lorenz system simulation. We simulated the Lorenz system⁹⁴,

$$\begin{aligned}\dot{s}_1 &= 10(s_2 - s_1) \\ \dot{s}_2 &= s_1(28 - s_3) - s_2 \\ \dot{s}_3 &= s_1s_2 - \frac{8}{3}s_3\end{aligned}$$

using MATLAB's `ode45` Runge-Kutta ordinary differential equation solver⁸³ with a time step $dt = 0.01$ s and error tolerances of 10^{-8} . We take the variable s_1 as the observation time series $y(t)$. To simulate a noisy observation process we add to $y(t)$ a uniform white noise with s.d. of 0.5% the s.d. of s_1 . The state space is reconstructed from the one-dimensional observed time series as described above (without the ICA step).

Choosing reconstruction parameters by maximizing predictability. To choose the reconstruction parameters (K, m) we first vary K in the range $1 \leq K \leq K_{\max}$ and estimate T_{pred} in the candidate state space \bar{Y}_K formed by the delayed observations. We set K^* as the minimum K where T_{pred} as a function of K begins to decrease. In cases where T_{pred} saturates but does not decrease, we choose K^* as the K at which T_{pred} saturates. If K_{\max} appears too short, then it can be increased step-wise until $T_{\text{pred}}(K)$ starts decreasing. For the Lorenz system we have $K_{\max} = 100$ frames, while for the worm data we have $K_{\max} = 30$ frames. Intuitively, K^* should allow the reconstruction to capture the fastest timescale of the system, which for chaotic systems is set by the period of the smallest UPO, p_{\min} . Increasing K^* further filters across longer periods, and in the limit $K \rightarrow \infty$ the SVD filter becomes a discrete Fourier transform⁹⁵. At the other end, K^* should be large enough to embed the dynamics completely. Using the bound given by Takens's embedding theorem^{25,30}, we obtain $(2m^* + 1)/d \leq K^* < p_{\min}$. Once the embedding window is set as K^* , we perform SVD $\bar{Y}_{K^*} = U\Sigma V^T$. The first m columns of U contain the normalized projections of \bar{Y}_{K^*} onto its first m singular vectors. To find the embedding dimension, we vary m and compute T_{pred} as above. We set the embedding dimension m^* as the minimum m where T_{pred} as a function of m saturates or begins to decrease.

Nearest-neighbour prediction. We estimate the τ -step future of an observation $y(t)$, denoted $y_{\text{est}}(t + \tau)$, from an average of the τ -step future of N_b nearest neighbours of the corresponding state-space point $x(t)$. Specifically, we find N_b nearest neighbours of $x(t)$ in state space, denoted by $z(t;r)$ for the r th nearest neighbour of $x(t)$, and average their values after τ steps, $x_{\text{est}}(t + \tau) = \langle z(t + \tau; r) \rangle_r$, for all N_b neighbours. Finally, we project $x_{\text{est}}(t + \tau)$ back to the observation space, to obtain $y_{\text{est}}(t + \tau)$. In delay space this is done by taking the first d columns of \bar{Y} , while in the SVD space we project back the m -dimensional prediction by $U_m \Sigma_m V_m^T$, where the subscript indicates that that these are m -dimensional truncations of the original matrices. To avoid trivially selecting the successive points as nearest neighbours, we take only the transverse nearest neighbours of $x(t)$, which are identified by the local minima of $R_r(t)$ estimated using the `findpeaks` function in MATLAB⁸³, where $R_r(t)$ is the distance between $x(t)$ and all other points in state space. We quantify the τ -step prediction accuracy by the root mean squared error

$$E(\tau) = \sum_{j=1}^d \langle (y_j(t + \tau) - (y_{\text{est}})_j(t + \tau))^2 \rangle_r^{1/2}$$

for $N = 10^4$ different test points $y(t)$ in the measurement time series. The predictions are made to a maximum prediction time, which is long enough that $E(\tau)$ saturates to e_s . Examples of $E(\tau)$ in different embedding dimensions are shown in Extended Data Fig. 9a,b for both the Lorenz system and an example worm. The root mean squared error is also a function of N_b . Making this dependence explicit, we write $E(\tau, N_b)$ when N_b is considered a variable. We set the number of neighbours by minimizing the one-step prediction error $E(1, N_b)$ (see Extended Data Fig. 10b for an example).

Calculation of T_{pred} . We developed a fixed-point algorithm to estimate T_{pred} . We begin with an initial guess of e_s labelled e_s^0 and time τ_s^0 such that $E(\tau) > e_s^0$ for all $\tau \geq \tau_s^0$. Next, noting that for large times $\int E(\tau) d\tau = e_s \tau - \Delta$, we fit a line to a numerical estimate of $\int E(\tau) d\tau$ from τ_s^0 to τ_{\max} . The slope of this line provides the next estimate of e_s , labelled e_s^1 , and the intercept is the next estimate of the area Δ , labelled Δ^1 . We use e_s^1 to again estimate τ_s^1 and fit a line to $\int E(\tau) d\tau$ from τ_s^1 to τ_{\max} , repeating the process until the estimates for e_s and Δ converge. Using the final estimates of Δ and e_s we can obtain a robust estimate $T_{\text{pred}} = \frac{\Delta}{e_s}$. A schematic of this iterative process is shown in Extended Data Fig. 9c. In our experience it only takes three or four iterations for the estimates to converge. To obtain the error bars we bootstrap across the prediction test points, generating 100 bootstrapped $E(\tau)$ curves along with T_{pred} estimates for each. These are then used to estimate the 95% confidence intervals of T_{pred} .

Prediction timescale T_{pred} . In cases where the error growth $E(\tau)$ is well approximated by a sigmoid (conjectured by Lorenz for chaotic systems with a single Lyapunov exponent λ ; ref. ³³), one can show $T_{\text{pred}} = \frac{1}{\lambda} \log\left(\frac{e_s}{e_1}\right)$, where e_1 is the one-time-step error $E(1)$. On the basis of information-theoretic considerations, Farmer⁹⁶ derived the upper bound for the predictability timescale as $\frac{D_i}{h_{KS}} \log\left(\frac{e_s}{e_1}\right)$, where D_i is the information dimension, which is consistent with our calculation for the sigmoid assumption. Importantly, these estimates shed light on the asymptotic behaviour of T_{pred} . For small values of K and m , the error is affected by some fraction of false nearest neighbours due to underembedding⁹⁷, leading to an overestimate of the local expansion rate and consequently the positive Lyapunov exponents. This causes a drop in T_{pred} via the $1/\lambda$ term. On the other hand, as we increase K , the average Euclidean distance between nearest neighbours e_1 steadily increases, leading to a

decrease in T_{pred} for high dimensions. This holds even when e_1 is measured in the measurement space; large distances in state space now correspond to differences in points that are separated by a time longer than the correlation time. In the middle of these two extremes we find a range of suitable values for the embedding window K . The SVD coordinates are weighted by decreasing singular values, which correspond to the variance of the data projected along the different singular vectors. In the noiseless case, the singular values decay towards zero, while in the presence of noise they decay before saturating to the s.d. of the noise (termed noise floor in ref. ²³), thus higher dimensions are generically dominated by noise in this case. Consequently, e_1 does not increase as a function of m in the noiseless case, leading T_{pred} to saturate after successful embedding. However, in the presence of noise e_1 increases, causing T_{pred} to go down. We note that our state space is defined by the left singular vectors of \tilde{Y} , which are unit norm.

Periodic orbits. The detection of periodic orbits from experimental data is made practical by various shadowing theorems, which state that any approximate orbit is shadowed by a true orbit of the dynamical system^{80,98,99}. We follow the steps described in previous work^{51,100,101} to detect periodic orbits of length p , and identify close recurrences in the state space. First, we utilize the function $\epsilon(r, t)$ as defined in ref. ¹⁰⁰, which gives the r th smallest distance between state-space points separated by time t . An example of this function for our data is shown in Extended Data Fig. 8a. The existence of periodic orbits is revealed when the local minima of $\epsilon(r, t)$ occur at regular intervals. The times at which the minima occur estimate the periods p , while $\epsilon(r, p)$ gives the minimum distance at which we must look to find a periodic orbit of length p . Consequently, any sequence $[\mathbf{x}(i), \mathbf{x}(i+1), \dots, \mathbf{x}(i+p)]$ where $\|\mathbf{x}(k) - \mathbf{x}(i)\| < \epsilon(r, p)$ is stored as a periodic orbit of length p . If $\epsilon(r, t)$ does not show any local minima, then periodic orbits cannot be detected from the data. We only consider transverse recurrences to avoid sequential points and we set $r = m^*$, the dimension of the reconstructed state space. In the Jacobian and maximal exponent calculations described below, ϵ is the distance corresponding to p_{\min} , the first local minimum of $\epsilon(r, t)$.

Maximum Lyapunov exponent λ_{\max} . Our test for the exponential divergence of neighbouring trajectories follows standard approaches¹⁰². Specifically, we consider a reference trajectory $\mathbf{x}(t' + \tau)$ and its nearest neighbours within a distance ϵ . (Periodic orbits). We then track the average distance between the reference and neighbouring trajectories over time to obtain the curve $\delta_r(\tau)$. A substantial linear region in the $\langle \log \delta_r(\tau) \rangle_r$ curve indicates an exponential divergence of neighbouring trajectories, while the slope of the linear region provides an estimate of λ_{\max} . There is typically a transient before the exponential growth where the perturbation vector aligns itself with the Lyapunov vector corresponding to the maximal exponent. In the Lorenz system this transient arises from the finite size of the perturbation and vanishes in the infinitesimal limit (Extended Data Fig. 10c,d). Notably, the behaviour of worms off food is not stationary; there is a slow increase in the tendency to make longer forward runs as time progresses. We address this by only considering the last 2 min of the recordings, where the behaviour can be considered approximately stationary.

Jacobian estimation. The Jacobian at the point $\mathbf{x}(i)$ in state space, denoted $J_{\mathbf{x}(i)}$, is the derivative of the dynamics at $\mathbf{x}(i)$, forming the local linear approximation of the dynamics at that point. We use a modified version of the Jacobian estimation algorithm described in ref. ¹⁰³, which solves a weighted regression problem $B_{\mathbf{x}(i)}^{-1} = B_{\mathbf{x}(i)} \cdot J_{\mathbf{x}(i)}$, where points are assigned weights according to their distance from $\mathbf{x}(i)$ as per the weighting function defined below. $B_{\mathbf{x}(i)}$ is a $(T - K^*) \times (m + 1)$ matrix containing all weighted state-space points concatenated with a column of ones, while $B_{\mathbf{x}(i)}^{-1}$ is a $(T - K^*) \times m$ matrix containing all weighted successors. Each row of $B_{\mathbf{x}(i)}$ and $B_{\mathbf{x}(i)}^{-1}$ is weighted by $w(k) = \exp\{-\frac{\|\mathbf{x}(i) - \mathbf{x}(k)\|}{\epsilon}\}$. The estimated local Jacobian matrix is then given by $J_{\mathbf{x}(i)} = B_{\mathbf{x}(i)}^{-1} \cdot B_{\mathbf{x}(i)}$, where $B_{\mathbf{x}(i)}^{-1}$ is the pseudoinverse of $B_{\mathbf{x}(i)}$, which we compute using the `pinv` function in MATLAB⁸³. Note that ϵ is the distance scale corresponding to the minimum period recurrence (Periodic orbits).

Lyapunov spectrum. To estimate the full spectrum of Lyapunov exponents, we calculate the long-time average (over the entire recording) of the estimated Jacobians by following the methods in refs. ^{104,105}. Specifically, the estimated Jacobians are used to track the evolution of a set of orthonormal vectors Q , by the recursive QR decomposition scheme $J_{\mathbf{x}_{i+1}} Q_i = Q_{i+1} R_{i+1}$, where $Q_0 = I$ is the $m \times m$ identity matrix. The j th Lyapunov exponent is then given by $\lambda_j = \frac{1}{\Delta t} \sum_{i=0}^{T-1} \log (R_i)_{jj}$ where $(R_i)_{jj}$ is the j th diagonal element of R_i and Δt is the sampling interval. The distribution of exponents in Fig. 5 and Extended Data Fig. 6b-d is obtained by bootstrapping the mean over all 12 foraging worms.

Floquet exponents. The real parts of the Floquet exponents of a periodic orbit, which measure their stability, are equal to the Lyapunov exponents of the orbit¹⁰⁶. Thus, to estimate the Floquet exponents of a periodic orbit, we estimate the maximal local Lyapunov exponent along the orbit using the procedure described in the previous section. This is done by restricting the above calculation over the length of a specific periodic orbit; that is, the Jacobians $J_{\mathbf{x}_{i+1}}$ are restricted to the Jacobians along a periodic orbit, and the averaging is performed for the duration of the periodic orbit, that is $\mu_1 = \frac{1}{\Delta t} \sum_{i=0}^{p-1} \log (\tilde{R}_i)_{11}$, where \tilde{R} indicates that the QR decomposition is only done for Jacobians along the periodic orbit.

Lyapunov exponents of random sequences. To calculate the exponents for short random sequences in Fig. 4c we proceed as above, but instead of performing the calculation over the entire recording we consider a trajectory starting at a random point in state space and follow it for the duration of a periodic orbit. Thus these sequences are the same length as a periodic orbit, but not necessarily recurrent.

Reporting Summary. Further information on research design is available in the Nature Research Reporting Summary linked to this article.

Data availability

Posture-mode time series for all worms analysed here are publicly available: <https://bitbucket.org/tosifahamed/behavioral-state-space>. Original image data for the foraging and escape-response datasets were analysed previously⁹ and are available from the Dryad Digital Repository: <https://doi.org/10.5061/dryad.t0m6p>. Data for N2 worms on food and *npr-1* mutants were collected from an open-access dataset⁸⁴ and analysed to solve for coiled postures¹¹. All other data that support the plots within this paper and other findings of this study are available from the corresponding author upon reasonable request.

Code availability

Code for all analysis reported here was written in MATLAB⁸³ and is publicly available: <https://bitbucket.org/tosifahamed/behavioral-state-space>.

References

83. MATLAB v9.3.0 (R2017b) (MathWorks, 2017).
84. Javer, A. et al. An open-source platform for analyzing and sharing worm-behavior data. *Nat. Methods* **15**, 645–646 (2018).
85. Sulston, J. E. & Brenner, S. The DNA of *C. elegans*. *Genetics* **77**, 95–104 (1974).
86. Brenner, S. The genetics of *Caenorhabditis elegans*. *Genetics* **77**, 71–94 (1974).
87. Yemini, E., Kerr, R. A. & Schafer, W. R. Preparation of samples for single-worm tracking. *Cold Spring Harb. Protoc.* **2011**, 1475–1479 (2011).
88. Casdagli, M., Sauer, T. & Yorke, J. A. Embedology. *J. Stat. Phys.* **65**, 579–616 (1991).
89. Stark, J., Broomhead, D. S., Davies, M. & Huke, J. Delay embeddings for forced systems. II. Stochastic forcing. *J. Nonlinear Sci.* **13**, 519–577 (2003).
90. Muldoon, M. R., Broomhead, D. S., Huke, J. P. & Hegger, R. Delay embedding in the presence of dynamical noise. *Dyn. Stab. Syst.* **13**, 175–186 (1998).
91. Stark, J. Delay embeddings for forced systems. I. Deterministic forcing. *J. Nonlinear Sci.* **9**, 255–332 (1999).
92. Huke, J. P. & Broomhead, D. S. Embedding theorems for non-uniformly sampled dynamical systems. *Nonlinearity* **20**, 2205 (2007).
93. Deyle, E. R. & Sugihara, G. Generalized theorems for nonlinear state space reconstruction. *PLoS ONE* **6**, e18295 (2011).
94. Lorenz, E. N. Deterministic nonperiodic flow. *J. Atmos. Sci.* **20**, 130–148 (1963).
95. Vautard, R. & Ghil, M. Singular spectrum analysis in nonlinear dynamics, with applications to paleoclimatic time series. *Physica D* **35**, 395–424 (1989).
96. Farmer, J. D. Information dimension and the probabilistic structure of chaos. *Z. Naturforsch. A* **37**, 1304–1326 (1982).
97. Kennel, M. B., Brown, R. & Abarbanel, H. D. I. Determining embedding dimension for phase-space reconstruction using a geometrical construction. *Phys. Rev. A* **45**, 3403–3411 (1992).
98. Hammel, S. M., Yorke, J. A. & Grebogi, C. Do numerical orbits of chaotic dynamical processes represent true orbits? *J. Complex.* **3**, 136–145 (1987).
99. Nusse, H. E. & Yorke, J. A. Is every approximate trajectory of some process near an exact trajectory of a nearby process? *Commun. Math. Phys.* **114**, 363–379 (1988).
100. Pawelzik, K. & Schuster, H. Unstable periodic orbits and prediction. *Phys. Rev. A* **43**, 1808 (1991).
101. Badii, R. et al. Progress in the analysis of experimental chaos through periodic orbits. *Rev. Mod. Phys.* **66**, 1389 (1994).
102. Kantz, H. A robust method to estimate the maximal Lyapunov exponent of a time series. *Phys. Lett. A* **185**, 77–87 (1994).
103. Deyle, E. R., May, R. M., Munch, S. B. & Sugihara, G. Tracking and forecasting ecosystem interactions in real time. *Proc. R. Soc. B* **283**, 20152258 (2016).
104. Abarbanel, H. D. I., Brown, R. & Kennel, M. B. Variation of Lyapunov exponents on a strange attractor. *J. Nonlinear Sci.* **1**, 175–199 (1991).
105. Abarbanel, H. D. I., Brown, R. & Kennel, M. B. Local Lyapunov exponents computed from observed data. *J. Nonlinear Sci.* **2**, 343–365 (1992).
106. Guckenheimer, J. & Holmes, P. *Nonlinear Oscillations, Dynamical Systems, and Bifurcations of Vector Fields* (Springer, 1983).

Acknowledgements

We thank D. Jordan, I. Etheredge and A. Celani for comments. L. Hebert (OIST Graduate University) developed the custom machine-learning solution for pose estimation of worms in on-food conditions. We would also like to express our gratitude to I. Maruyama for his support during the project. This work was supported by OIST Graduate University (T.A., G.J.S.), a programme grant from the Netherlands Organization for Scientific Research (A.C.C., G.J.S.), Vrije Universiteit Amsterdam (G.J.S.) and the Japan Society for the Promotion of Science (T.A.).

Author contributions

T.A., A.C.C. and G.J.S. designed the research, performed the research, analysed the data and wrote the paper.

Competing interests

The authors declare no competing interests.

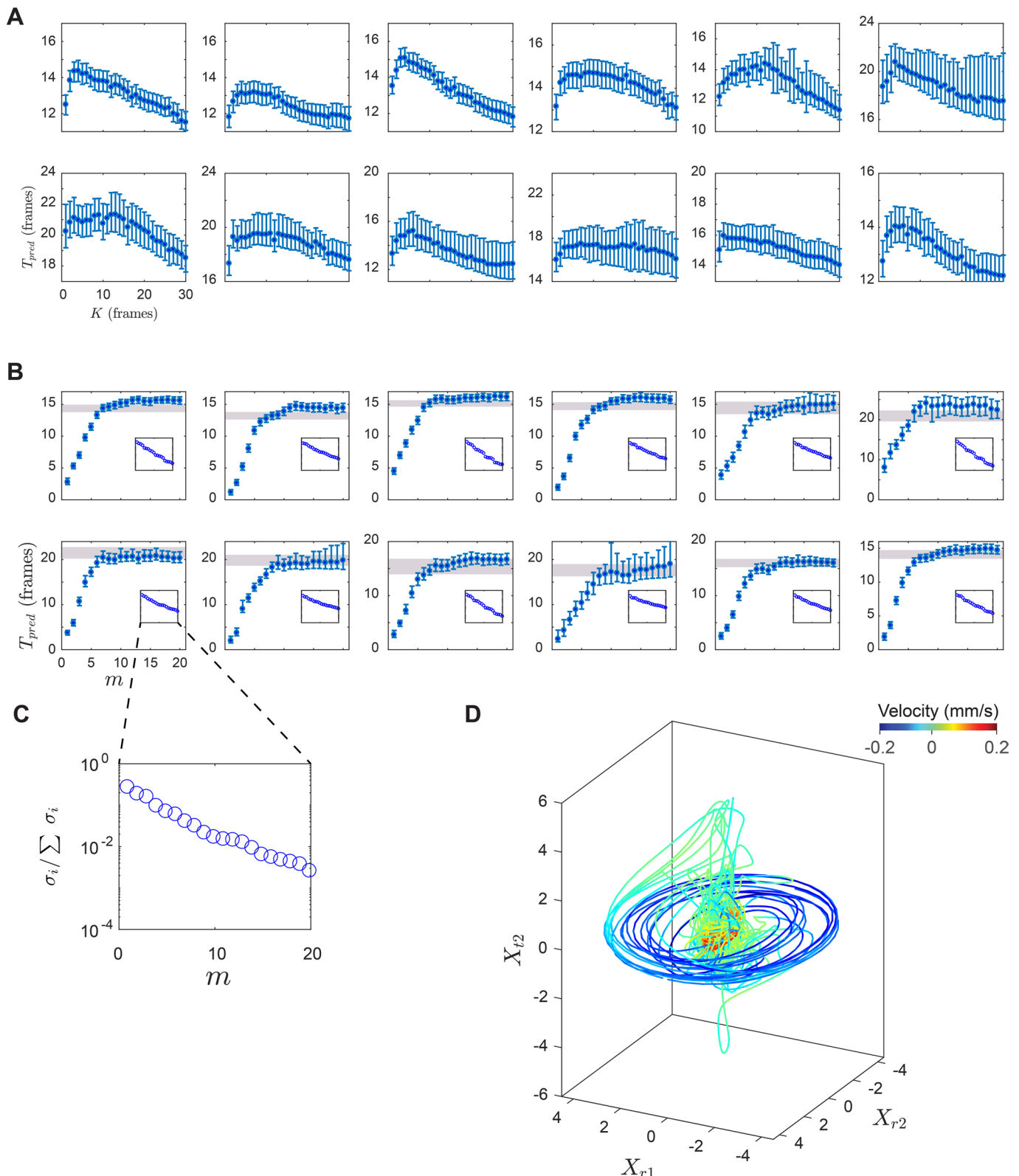
Additional information

Extended data is available for this paper at <https://doi.org/10.1038/s41567-020-01036-8>.

Supplementary information is available for this paper at <https://doi.org/10.1038/s41567-020-01036-8>.

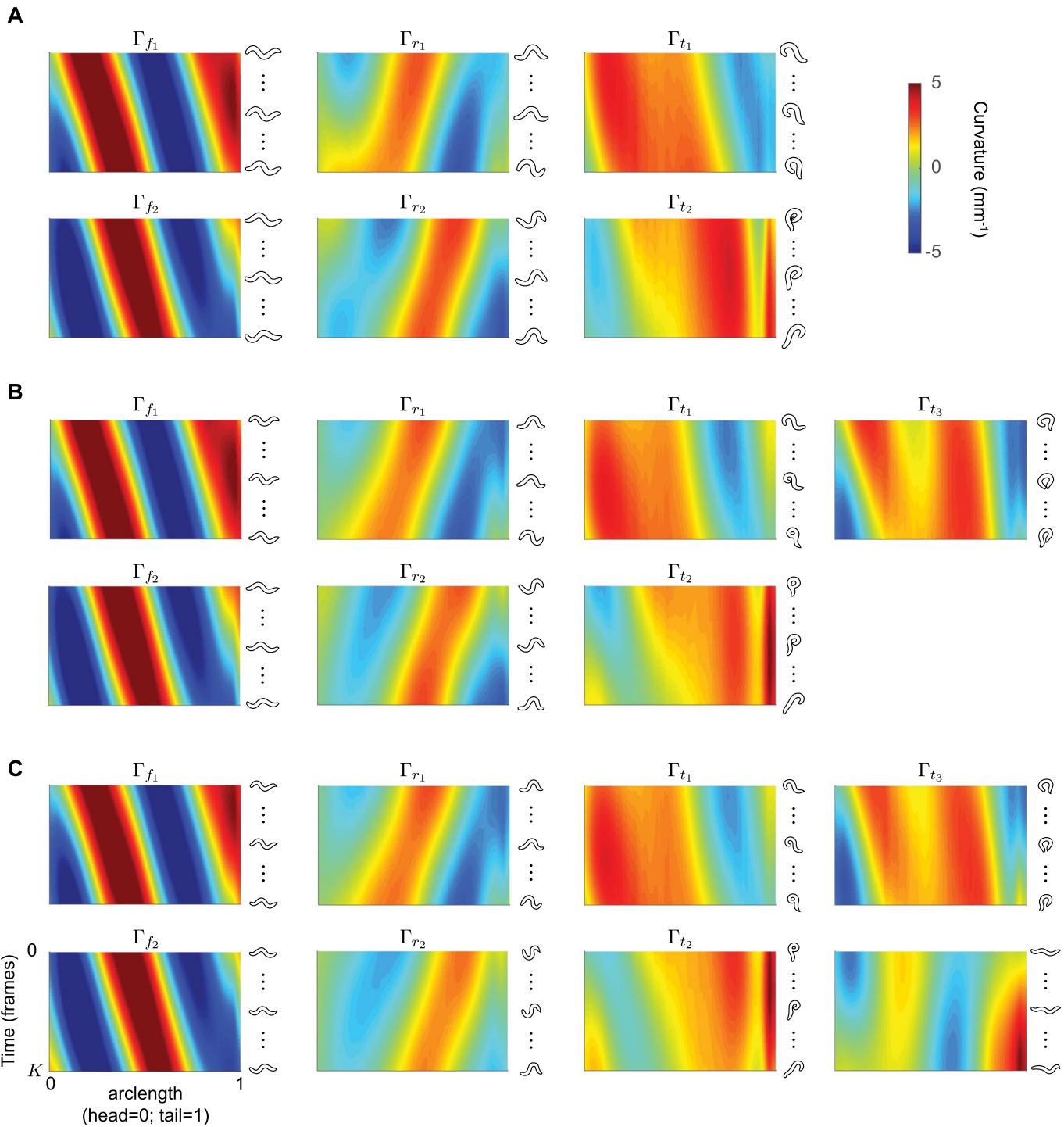
Correspondence and requests for materials should be addressed to G.J.S.

Reprints and permissions information is available at www.nature.com/reprints.

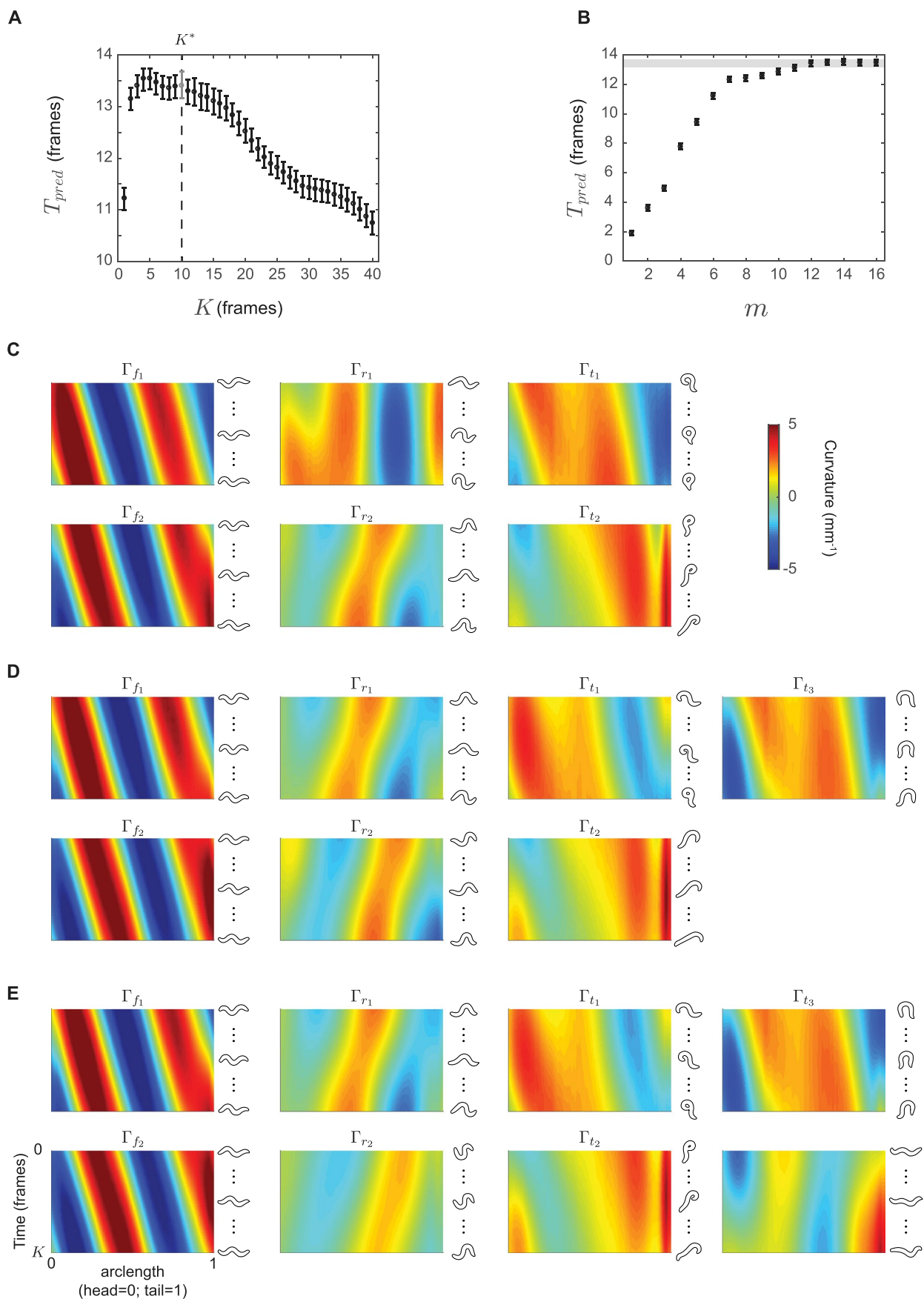


Extended Data Fig. 1 | The predictability T_{pred} as a function of K and m for $N = 12$ individual worms. **a**, T_{pred} as a function of K . **b**, T_{pred} as a function of m .

We find similar curves across worms, despite the differences in their detailed dynamics. Note that while the distance metric in the SVD space (**b**) and the space of delays (**a**) is different, which could result in inconsistencies in the estimation of T_{pred} , we find only minor differences between the maximum T_{pred} in the two cases (gray bar in B). Inset shows the normalized singular value spectrum, which does not have a clear cutoff for any worm. **c**, Expanded inset in B showing the normalized singular value spectrum. **d**, State space captures a commonly observed sequence where long reversals transition to forward via a deep body bends seen here as a large excitation in X_{t2} as the reversal ends. Here we see that the blue (backward) and red (forward) bundles are smoothly connected via a large transient along the turning mode X_{t2} (data from the example worm in Fig. 3b–e).

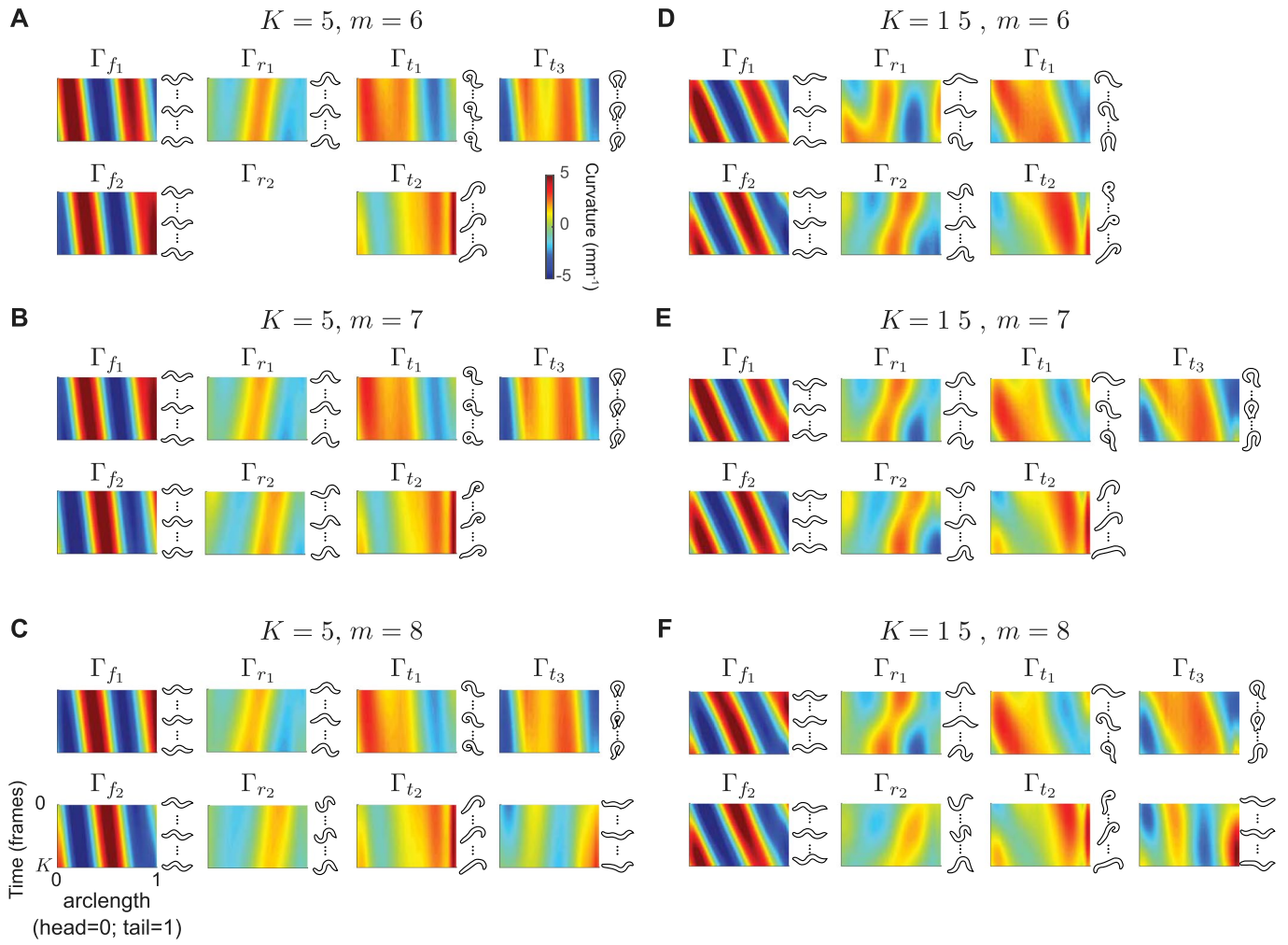


Extended Data Fig. 2 | Dominant state space modes are stable across different embedding dimensions, with distinct groups independently capturing forward, reversal and turning behaviors. **a-c**, Behavioral modes estimated for the worm in Fig. 3 for dimensions, $m = 6$ (**a**), $m = 7$ (**b**), and $m = 8$ (**c**); embedding window is set to $K = 12$ frames. The modes retain their interpretability across dimensions. In a 6-dimensional embedding, there are two forward, two backward and two turning modes. In 7 dimensions one of the turning modes further splits into an omega-turn like mode (Γ_{t_3}) and a delta-turn like mode (Γ_{t_1}), while Γ_{t_2} changes little. Furthermore, the reversal modes are more separable in 7 dimensions. The 8-dimensional state space retains the forward, reversal and turning dynamics along with an additional and subtle head-bending.

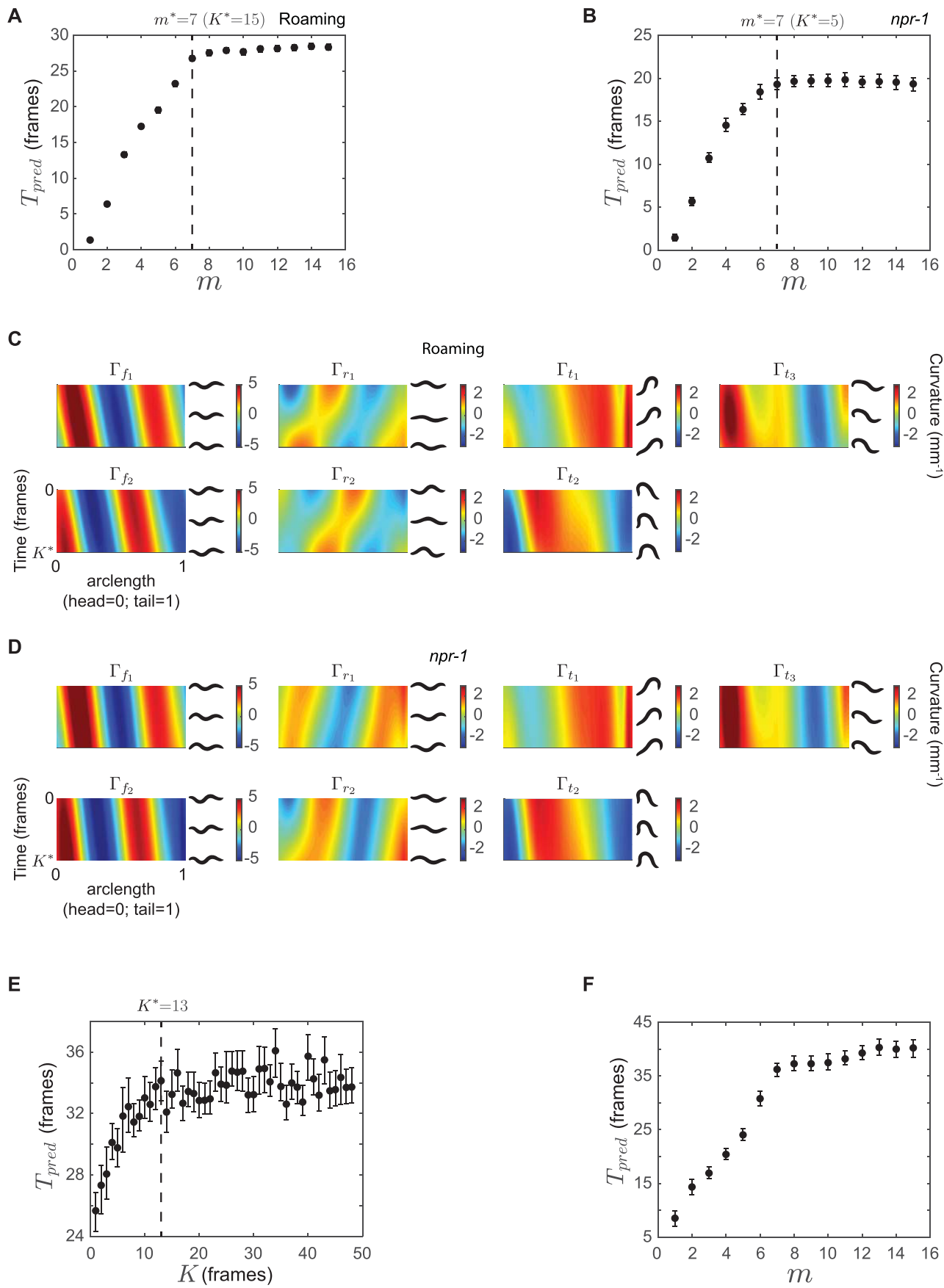


Extended Data Fig. 3 | See next page for caption.

Extended Data Fig. 3 | The ensemble embedding across all $N = 12$ worms is constructed from their concatenated posture time series and characterized by $K^* = 10$ and $m^* = 7$. **a–b**, T_{pred} as a function of K and m . We set $K^* = 10$, approximately when T_{pred} begins to decrease, and show $T_{\text{pred}}(m)$ at this K^* . We show the resulting modes for $m = 6$ and the gray bar denotes $T_{\text{pred}}(K = K^*)$. **c**, $m = 7$ (**d**), and $m = 8$ (**e**), and these are qualitatively similar to those obtained from our representative worm of Extended Data Fig. 2. The additional modes present for embeddings greater than $m^* = 7$ offer only minor improvements in predictability.



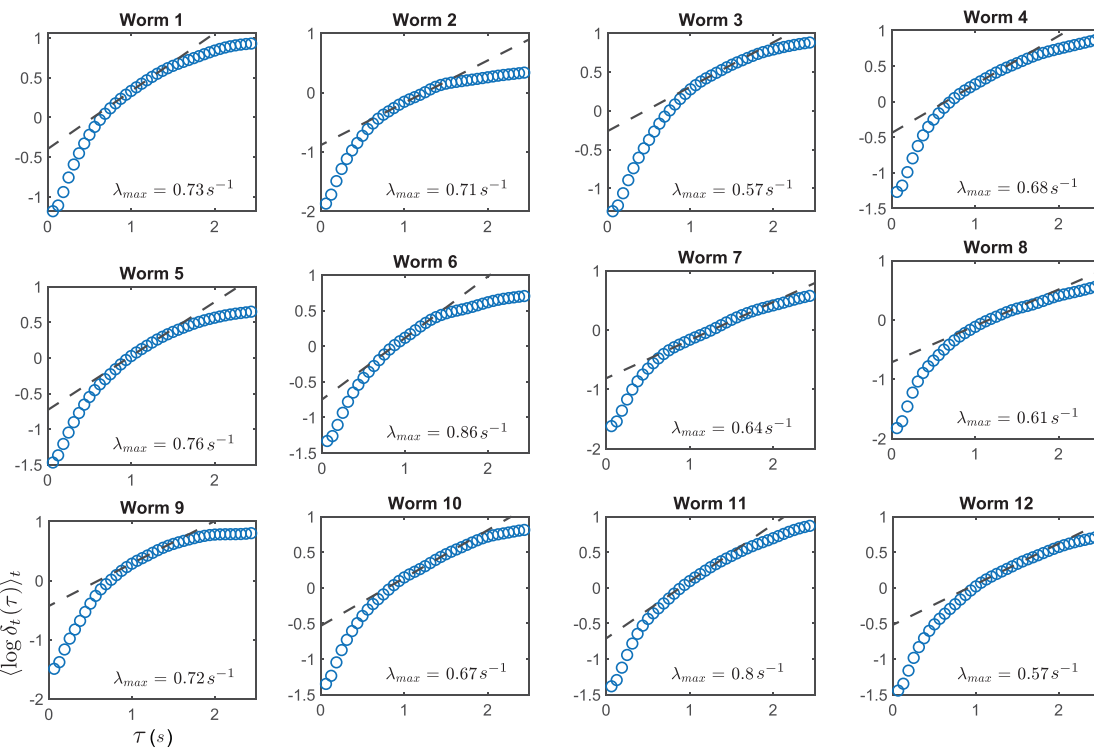
Extended Data Fig. 4 | Ensemble embedding for different values of K and m . **a–c**, Behavioral modes estimated from the ensemble for $K = 5$, and dimensions, $m = 6$ (**a**), $m = 7$ (**b**), and $m = 8$ (**c**). **d–f**, Same as above but for $K = 15$. The modes are qualitatively similar across this variation.



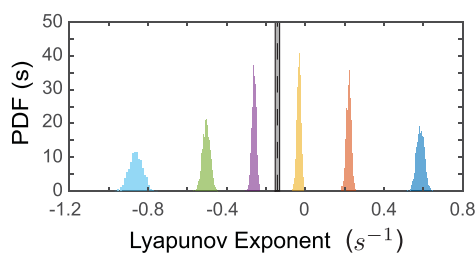
Extended Data Fig. 5 | See next page for caption.

Extended Data Fig. 5 | The dominant off-food modes are similar to those of on-food roaming behavior and on-food behavior of *npr-1* mutant worms.

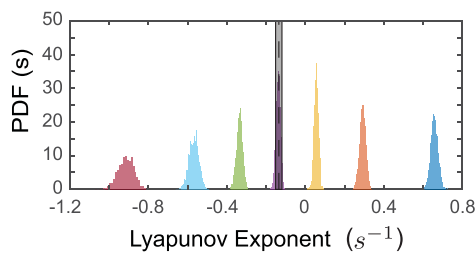
We analyze a collection of $N = 25$ on-food ‘roaming’ N2 worms, $N = 25$ on-food ‘dwelling’ N2 worms, and $N = 7$ on-food mutant *npr-1* worms from an open access dataset⁸⁴ (Methods, see also Extended Data Fig. 10a). We show $T_{\text{pred}}(m)$ for (a) on-food N2 roaming worms and (b) on-food *npr-1* mutants. c-d, Kymographs of the $m^* = 7$ primary modes from roaming and *npr-1* worms coincide, both with each other and with the off-food N2 modes in Fig. 3. The similarity of these embeddings provide new, posture-scale evidence that the NPR-1 mutation overrides the switch to dwelling⁴⁵. e-f, The combined embedding of roaming-dwelling on-food behavior exhibits an additional ~ 6 modes with small but notable additional T_{pred} , which was also observed in off-food behavior in the ensemble embedding, Extended Data Fig. 3, and for some individual worms, Extended Data Fig. 1b.

A**B****6 Dimensional Embedding**

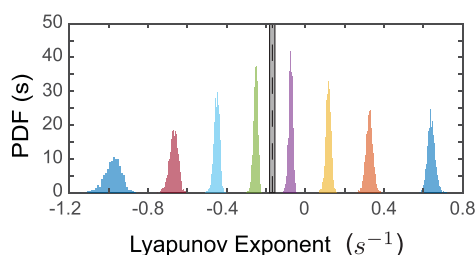
- λ_1
- λ_2
- λ_3
- $\lambda_4 = \lambda_3^* \approx \alpha - \lambda_3$
- $\lambda_5 = \lambda_2^* \approx \alpha - \lambda_2$
- $\lambda_6 = \lambda_1^* \approx \alpha - \lambda_1$
- - - $\alpha/2$

**C****7 Dimensional Embedding**

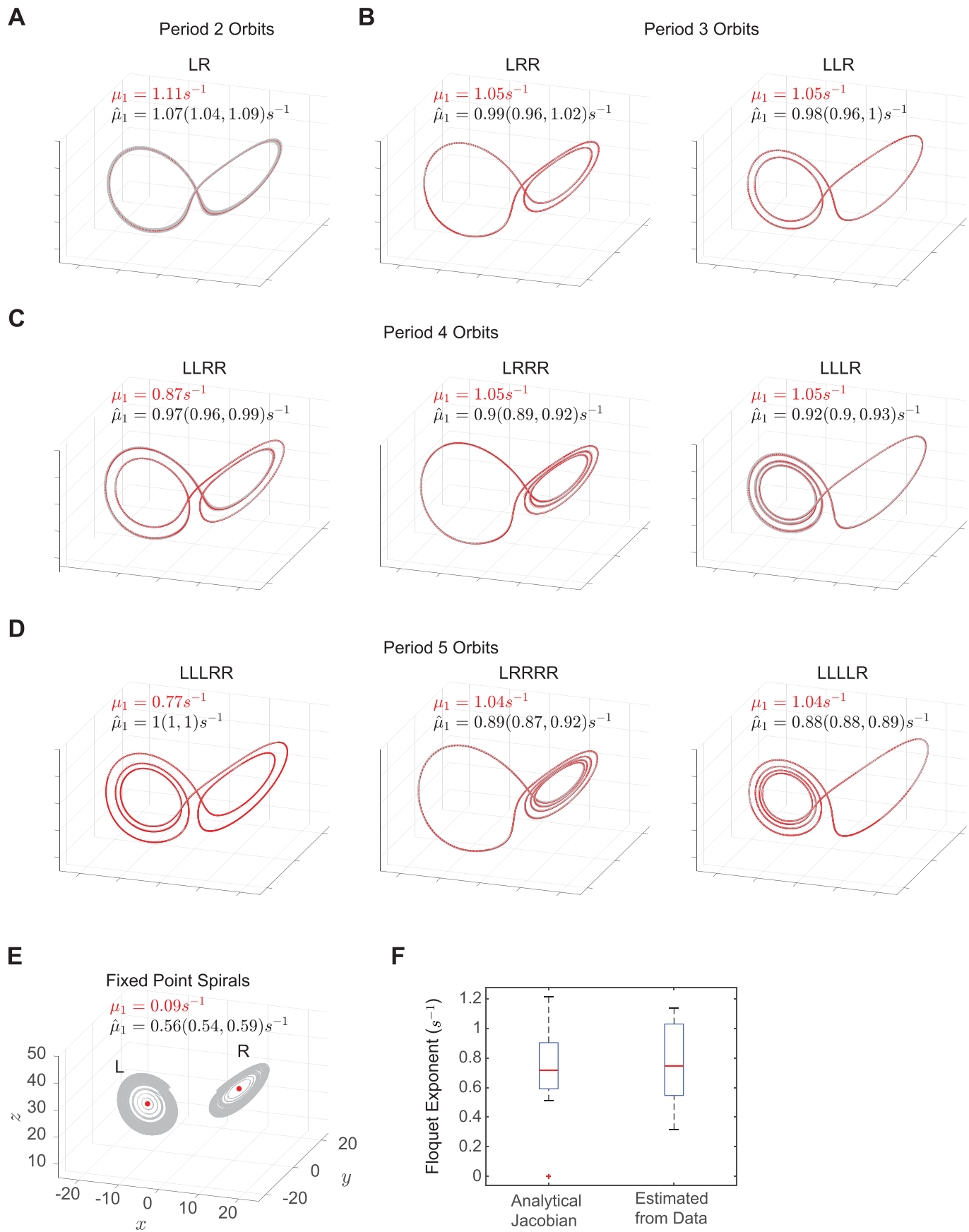
- λ_1
- λ_2
- λ_3
- λ_4
- $\lambda_5 = \lambda_3^* \approx \alpha - \lambda_3$
- $\lambda_6 = \lambda_2^* \approx \alpha - \lambda_2$
- $\lambda_7 = \lambda_1^* \approx \alpha - \lambda_1$
- - - $\alpha/2$

**D****8 Dimensional Embedding**

- λ_1
- λ_2
- λ_3
- λ_4
- $\lambda_5 = \lambda_4^* \approx \alpha - \lambda_4$
- $\lambda_6 = \lambda_3^* \approx \alpha - \lambda_3$
- $\lambda_7 = \lambda_2^* \approx \alpha - \lambda_2$
- $\lambda_8 = \lambda_1^* \approx \alpha - \lambda_1$
- - - $\alpha/2$

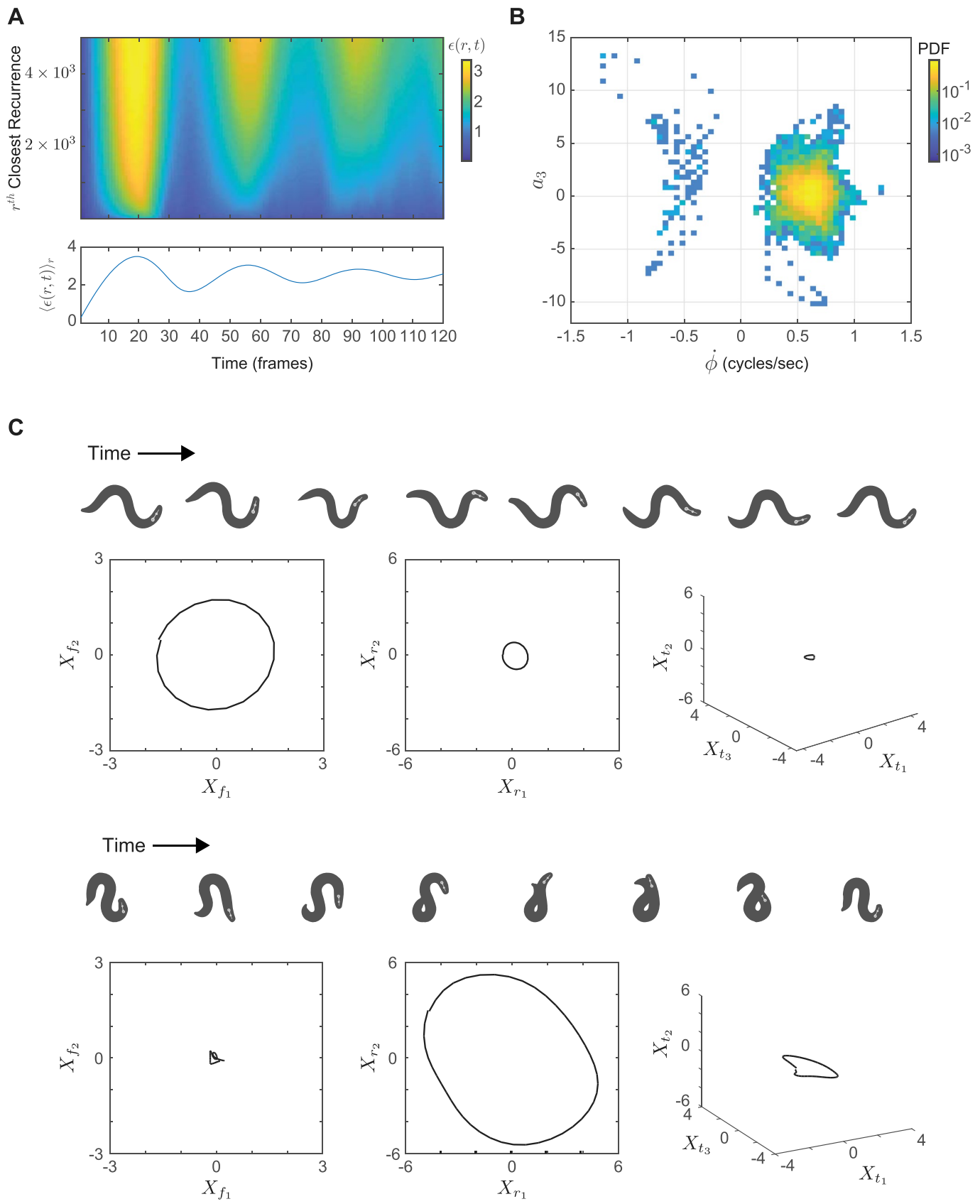
**Extended Data Fig. 6 | See next page for caption.**

Extended Data Fig. 6 | Maximum Lyapunov exponent for different worms and the full Lyapunov spectrum in different embedding dimensions. **a**, To quantify the state space divergence we plot the logarithm of the average distance between a trajectory and its nearest neighbors, averaged over several starting reference trajectories. For each worm we find that, after a transient, there is linear region showing exponential divergence. The slope of the linear region provides an estimate of the maximal Lyapunov exponent λ_{max} and the positive exponents are an indication of chaos in worm behavior. **b-d**, Lyapunov spectra computed from reconstructions of worm behavior in different embedding dimensions. Conjugate pairing of Lyapunov exponents is robustly observed in dimensions 6 and above.



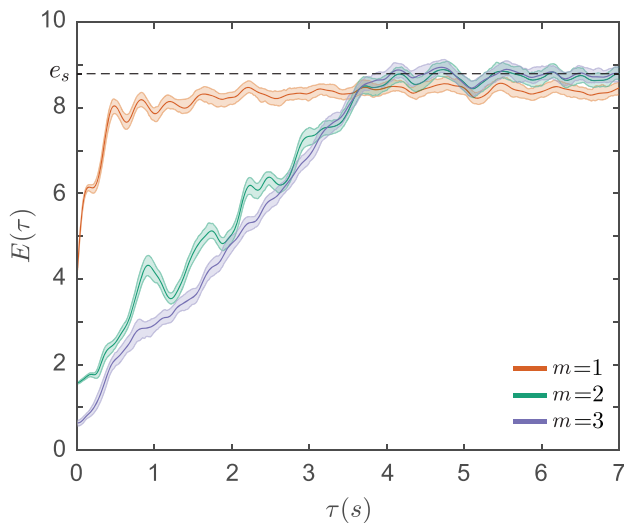
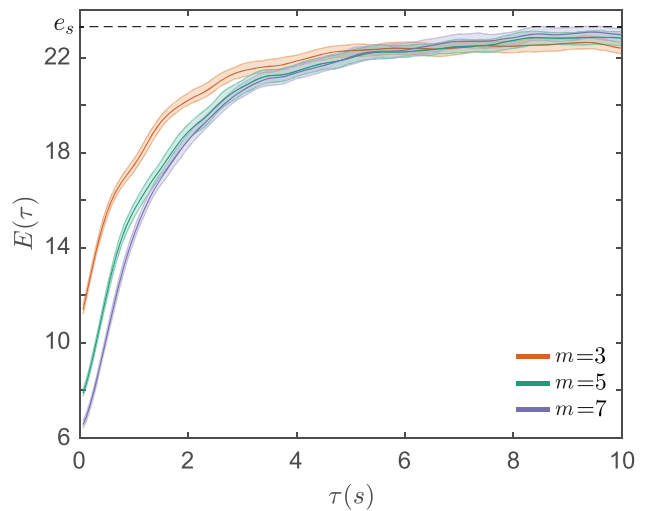
Extended Data Fig. 7 | See next page for caption.

Extended Data Fig. 7 | Detecting periodic orbits in the Lorenz System. **a–e**, We compare UPO trajectories for the Lorenz system computed from high precision numerical estimates⁵² (red) with periodic orbits detected using our recurrence based approach (grey) (only 3 UPOs are shown for period 5). The closely-matching trajectories also exhibit agreement between the Floquet exponents estimated from analytical Jacobians (red text) and Local Lyapunov exponents obtained from the estimated Jacobians (grey text). Note that in **(e)**, a fixed point (period-0 orbit) can only be detected by neighboring spiraling trajectories, leading to an overestimation of the exponent. **f**, Boxplot comparing the entire distribution of Floquet exponents for UPOs up to period 10 (red bars denote the median).

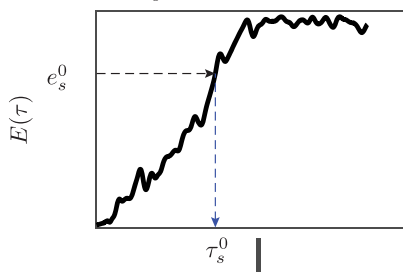


Extended Data Fig. 8 | See next page for caption.

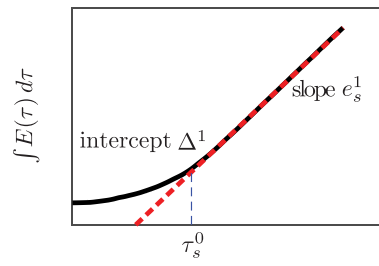
Extended Data Fig. 8 | Recurrence Function and Period-1 UPOs. **a**, The recurrence function $\epsilon(r, t)$ from the same worm in Fig. 3 for 120 frames and 5000 closest recurrences (top). Local minima of this function at times t , as seen in the average $\langle \epsilon(r, t) \rangle$, shown below correspond to close recurrences and identify periodic orbits of length t . The first local minimum is the smallest period p_{min} which is 37 frames in this example. For a given value of r , $\epsilon(r, t)$ gives the distance threshold at which we must look to find a periodic orbit of length t . **b**, Probability distribution of phase velocities $\dot{\phi}$ and third eigenwurm coefficient a_3 , which is proportional to mean body curvature, across all period-1 orbits of duration p_{min} from all worms in the dataset. We see two clusters corresponding to forward and backward locomotion, as well as orbits with a dorsal or ventral bias (for example orbits at bottom right and top left). **c**, Example period-1 orbits from the same worm in (a) corresponding to forward (top) and backward (bottom) locomotion.

A**B****C**

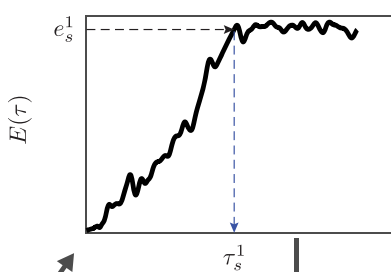
Start with an initial guess of e_s labeled e_s^0 and find corresponding time τ_s^0



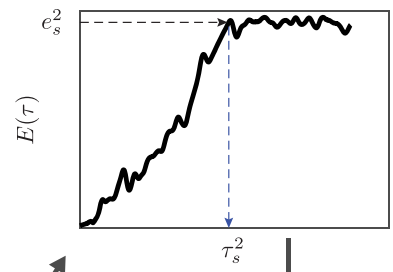
Fit a line to $\int E(\tau) d\tau$ starting from τ_s^0 , slope is a new estimate of e_s labeled e_s^1 , while the intercept estimates the area Δ



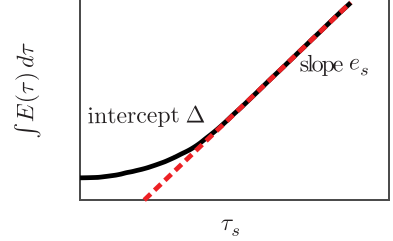
Find corresponding time τ_s^1 , for e_s^1



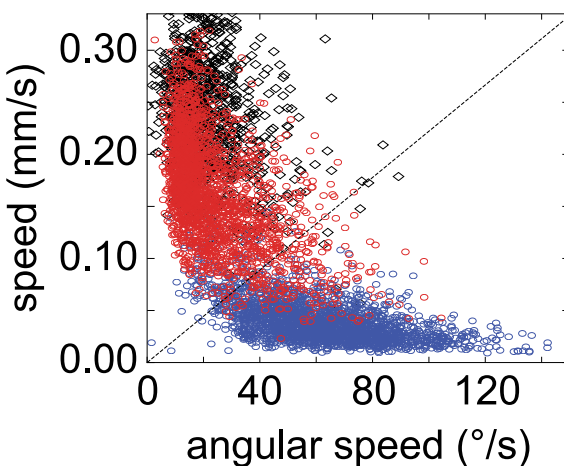
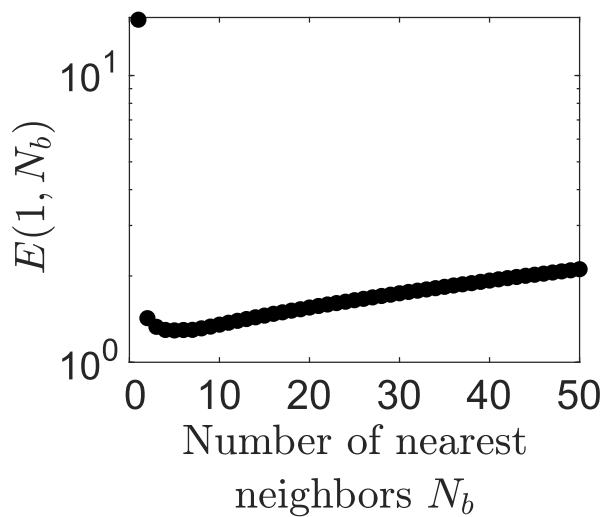
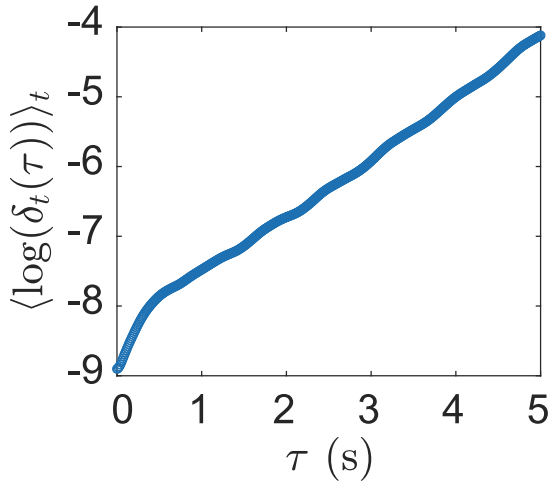
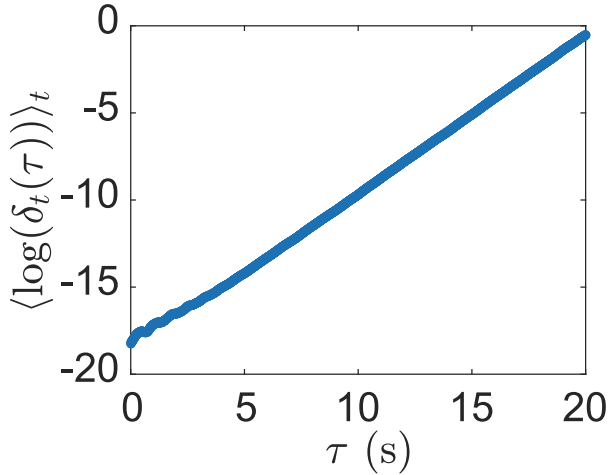
Fit a line to $\int E(\tau) d\tau$ starting from τ_s^1 to get new estimates and repeat until they converge.



Get final estimates



Extended Data Fig. 9 | Example $E(\tau)$ curves. **a**, Error curves are plotted for different embedding dimensions for the Lorenz system state space reconstruction ($K^* = 25$). **b**, Error curves in different embedding dimensions for the sample worm in Fig. 3b–e. Better embeddings lead to a lower error curve. The ratio of the area between these curves and the saturation value e_s to e_s estimates T_{pred} . **c**, A schematic showing the fixed point algorithm for robust estimation of the asymptote e_s , and the area Δ .

A**B****C****D**

Extended Data Fig. 10 | Roaming/dwelling states and further embedding details. **a**, Centroid speed and angular speed (averaged in 10 s windows) for the collection of worms used in the N2 on food dataset (red and blue) and the *npr-1* dataset (black). We initially collected 150 recordings of N2 worms crawling on food-full plates from an open dataset⁸⁴. From these, we selected 25 worms with a large fraction of dwelling states (blue) and 25 worms with a large fraction of roaming states (red), defined as in¹⁷. We downsample the data to 3 Hz (consistent with¹⁷), and average the centroid speed and angular speed in 10 s windows. Roaming and dwelling states are identified by a threshold defined by the line $y = x/450$ in the plane defined by x , the angular speed, and y , the centroid speed. Points above the line (high speed and low angular speed) are classified as roaming, while points below the line (low speed and high angular speed) are classified as dwelling. Data from *npr-1* mutants (black) show predominantly roaming behavior, consistent with previous reports⁴⁵. **b**, Example of the one step error, $E(1, N_b)$ curve used to pick the number of nearest neighbors. This was calculated on the same worm as in Fig. 3b-e. **c**, A transient can be seen for the Lorenz system before the linear regime indicating exponential growth of local finite-sized perturbations (sized $\approx 10^{-4}$) begins. **d**, Transient decreases when perturbations of size $\approx 10^{-8}$ are used.

Corresponding author(s): Greg J Stephens

Last updated by author(s): 7/20/2020

Reporting Summary

Nature Research wishes to improve the reproducibility of the work that we publish. This form provides structure for consistency and transparency in reporting. For further information on Nature Research policies, see [Authors & Referees](#) and the [Editorial Policy Checklist](#).

Statistics

For all statistical analyses, confirm that the following items are present in the figure legend, table legend, main text, or Methods section.

n/a Confirmed

- The exact sample size (n) for each experimental group/condition, given as a discrete number and unit of measurement
- A statement on whether measurements were taken from distinct samples or whether the same sample was measured repeatedly
- The statistical test(s) used AND whether they are one- or two-sided
Only common tests should be described solely by name; describe more complex techniques in the Methods section.
- A description of all covariates tested
- A description of any assumptions or corrections, such as tests of normality and adjustment for multiple comparisons
- A full description of the statistical parameters including central tendency (e.g. means) or other basic estimates (e.g. regression coefficient) AND variation (e.g. standard deviation) or associated estimates of uncertainty (e.g. confidence intervals)
- For null hypothesis testing, the test statistic (e.g. F , t , r) with confidence intervals, effect sizes, degrees of freedom and P value noted
Give P values as exact values whenever suitable.
- For Bayesian analysis, information on the choice of priors and Markov chain Monte Carlo settings
- For hierarchical and complex designs, identification of the appropriate level for tests and full reporting of outcomes
- Estimates of effect sizes (e.g. Cohen's d , Pearson's r), indicating how they were calculated

Our web collection on [statistics for biologists](#) contains articles on many of the points above.

Software and code

Policy information about [availability of computer code](#)

Data collection

All analysis in this study uses data previously published in <https://doi.org/10.7554/eLife.17227> and from the Open Worm Movement Database <https://doi.org/10.1038/s41592-018-0112-1>.

Data analysis

Data analysis was performed using custom scripts written in Matlab and is available at <https://bitbucket.org/tosifahamed/behavioral-state-space/src/> where we also provide shape mode timeseries and canonical eigenworms

For manuscripts utilizing custom algorithms or software that are central to the research but not yet described in published literature, software must be made available to editors/reviewers. We strongly encourage code deposition in a community repository (e.g. GitHub). See the Nature Research [guidelines for submitting code & software](#) for further information.

Data

Policy information about [availability of data](#)

All manuscripts must include a [data availability statement](#). This statement should provide the following information, where applicable:

- Accession codes, unique identifiers, or web links for publicly available datasets
- A list of figures that have associated raw data
- A description of any restrictions on data availability

All data used in the manuscript is publicly available with unrestricted access

Field-specific reporting

Please select the one below that is the best fit for your research. If you are not sure, read the appropriate sections before making your selection.

Life sciences

Behavioural & social sciences

Ecological, evolutionary & environmental sciences

For a reference copy of the document with all sections, see nature.com/documents/nr-reporting-summary-flat.pdf

Life sciences study design

All studies must disclose on these points even when the disclosure is negative.

Sample size	No sample size calculation was performed as our analysis is based on previously published data.
Data exclusions	No data was excluded from the analysis.
Replication	The analysis was replicated on different animals in the dataset with little variation. Invariant measures such as Lyapunov exponents calculated by different methods were found to be within error bars. Finally, some of the analysis was reproduced by the coauthors and other members of the lab.
Randomization	Samples were not allocated into experimental groups. Randomization was used to estimate confidence intervals of reported measures.
Blinding	Blinding was not required for the analysis reported here because the data was not separated into groups.

Reporting for specific materials, systems and methods

We require information from authors about some types of materials, experimental systems and methods used in many studies. Here, indicate whether each material, system or method listed is relevant to your study. If you are not sure if a list item applies to your research, read the appropriate section before selecting a response.

Materials & experimental systems

- | | |
|-------------------------------------|-----------------------------|
| n/a | Involved in the study |
| <input checked="" type="checkbox"/> | Antibodies |
| <input checked="" type="checkbox"/> | Eukaryotic cell lines |
| <input checked="" type="checkbox"/> | Palaeontology |
| <input type="checkbox"/> | Animals and other organisms |
| <input checked="" type="checkbox"/> | Human research participants |
| <input checked="" type="checkbox"/> | Clinical data |

Methods

- | | |
|-------------------------------------|------------------------|
| n/a | Involved in the study |
| <input checked="" type="checkbox"/> | ChIP-seq |
| <input checked="" type="checkbox"/> | Flow cytometry |
| <input checked="" type="checkbox"/> | MRI-based neuroimaging |

Animals and other organisms

Policy information about [studies involving animals](#); [ARRIVE guidelines](#) recommended for reporting animal research

Laboratory animals	All the experiments were performed on young adults of <i>Caenorhabditis elegans</i> N2 and npr-1 strains
Wild animals	The study did not involve wild animals
Field-collected samples	The study did not involve samples collected from the field
Ethics oversight	No ethics oversight was needed because the research was done on <i>Caenorhabditis elegans</i>

Note that full information on the approval of the study protocol must also be provided in the manuscript.